Processing map for controlling microstructure and unraveling various deformation mechanisms during hot working of CoCrFeMnNi high entropy alloy

Madan Patnamsetty[1*], Mahesh C. Somani[2], Sumit Ghosh[2], Shahroz Ahmad[1], Pasi Peura[1]

[1]Materials Science and Environmental Engineering, Tampere University, 33720, Tampere, Finland
[2]Materials and Mechanical Engineering, Centre for Advanced Steels Research, University of Oulu, 90014, Finland

[*]Corresponding Author: madan.patnamsetty@tuni.fi

Abstract.

In the current study, the hot deformation characteristics and workability of a CoCrFeMnNi high entropy alloy was characterized using processing maps developed on the basis of dynamic materials model in the temperature range 1023 – 1423K and strain rate range 10^{-3} – $10s^{-1}$. The processing map delineated various deterministic domains including those of cracking processes and unstable flow, thus enabling identification of a 'safe' processing window for the hot working of the alloy. Accordingly, a deterministic domain in the temperature and strain rate ranges of 1223 – 1373K and 10^{-2} – $5\times10^{-1}s^{-1}$, respectively, was identified to be the domain of dynamic recrystallization (DRX) with a peak efficiency of the order of ~34% at 1293K and $3\times10^{-2}s^{-1}$ and these were considered to be the optimum parameters for hot deformation. The DRX grain size was dependent on the deformation temperature and strain rate, increasing with the increase in temperature and decrease in strain rate, whereas DRX volume increased with the strain rate. At still higher temperatures (1403 – 1423K) and lower strain rates (10^{-3} – $3\times10^{-3}s^{-1}$), there was a sharp decrease in efficiency values from 27% to 5% thus forming a trough and the microstructure was characterized with coarse grains. In the instability regime, grain boundary cracking/sliding and localized shear bands manifested at temperatures <1223K and strain rates $<10^{-2}s^{-1}$. The increase in strain rate resulted in an intense adiabatic shear banding along with formation of voids. At $10s^{-1}$ and temperatures >1398K, microstructural reconstitution occurred in the shear bands leading to the formation of fine grains, presumably as a consequence of continuous recrystallization.

Keywords: High entropy alloy, Dynamic materials model, Processing Map, Hot deformation, Dynamic Recrystallization, Instabilities

1. Introduction:

High entropy alloys (HEAs) are multi-metallic materials, comprising four or more principle alloying elements in equiatomic or near-equiatomic proportions [1,2]. In recent years, new alloy design concepts of multicomponent HEA systems have opened new avenues of research in order to explore a wide range of extraordinary properties. Li et al. [2] studied different combinatorial alloy designing techniques and reported that the approach to initial alloy design of HEAs was achieved through single phase solid solution. A high entropy of mixing accompanying a disordered solution of several elements was presumed to compete with the enthalpy of phase formation. It has been mentioned that there are multiple variants in design approaches, which include multiphases, formation of intermetallics and precipitates [2]. Miracle et al. [3] have reviewed a significant number of research works dedicated to the development and characterization of HEAs encompassing the alloy design, microstructural evolution, mechanical properties, and potential applications. Accordingly, the equiatomic CoCrFeMnNi alloy, which forms a disordered single FCC phase [2,3] happens to be the most studied HEA. This alloy is also called as 'Cantor alloy' named after Prof. Brian Cantor, who first invented it [4]. It was later discovered by Otto et al. [5] that prolonged annealing of Cantor alloy for 500 days below 1073K decomposed it into metallic Cr – Body centered cubic (BCC) and

intermetallic phases like $L1_0$-NiMn and B2-FeCo. These decomposition transformations are very quick in the case of nanocrystalline state [6], but take longer time for coarse grained structure [7]. However, based on various experimental results, George et al. [8] clarified that the heat treatments above 1073K, invariably retained the FCC phase in CoCrFeMnNi HEA at lower temperatures at normal cooling rates. The processing of CoCrFeMnNi HEA through cold rolling followed by annealing in the temperature range 673 – 1273K has shown the evolution of annealing twins in the microstructures [9]. The hot deformation of CoCrFeMnNi HEA at high temperatures (1023 – 1123K) at low strain rates (3.205×10^{-5}, 1.603×10^{-4} and $8.013\times10^{-4}s^{-1}$) has shown that the deformation is controlled by dislocation climb and the slowest diffusing species Ni controls the process rate [10]. Stepanov et al. [11] reported the occurrence of dynamic recrystallization (DRX) associated with nucleation of new grains along the initial grain boundaries and resulted in the increase of grain size with increase in temperature, during hot deformation (1073 – 1373K and 10^{-1}, $10^{-3}s^{-1}$),whilst the warm deformation (873 – 1073K and 10^{-1}, $10^{-3}s^{-1}$) led to the occurrence of DRX in adiabatic shear bands of CoCrFeMnNi HEA [11]. Additionally, Eleti at el. [12] reported significant grain refinement through DRX along the initial grain boundaries during hot compression (1073 – 1273K and 10^{-3}, 10^{-2}, $1s^{-1}$) of CoCrFeMnNi HEA and the grain size increased with increase in temperature and decrease in strain rate. Therefore, it is important to optimize the processing parameters to facilitate a defect free microstructure.

The workability of materials undergoing hot deformation is generally found to reduce significantly, if processed under non-optimal conditions of temperature and strain rates [13]. This is commonly attributed to the manifestation of plastic instabilities, such as formation of adiabatic shear bands, or occurrence of cracking processes, such as wedge cracks, intercrystalline cracks, surface cracks, etc. Although, a wide spectrum of defects may affect hot workability during the occurrence of dynamic processes, optimized processing under ideal deformation conditions over certain temperature and strain rate ranges, could enhance the processing efficiency through the facilitation of safe mechanisms, such as dynamic recrystallization (DRX) and dynamic recovery (DRV) [14]. Therefore, a complete characterization of workability is inevitably necessary for the optimization of hot working conditions of HEAs and realization of defect-free products.

Several microstructural changes (mechanisms) occur within the material as a response to the applied process parameters during deformation. Processing maps developed by Raj et al. [15] along the lines of the deformation mechanism maps of Ashby et al. [16] are considered valuable as they consider broad strain rate regimes, thus suggesting possibilities of the occurrence of wedge cracking at the triple junctions of the grain boundary (GB) at high temperature and low strain rates, and the occurrence of cavitation at low temperatures and high strain rates. These maps also account for the flow localization due to adiabatic shear banding. When all these mechanisms are taken into account, an area considered ‘safe’ for processing, such as DRX, can be easily delineated. In this context, an important development in understanding the constitutive flow behavior was advent of the processing map theory based on the principles of dynamic materials modelling (DMM) proposed by Prasad et al. [17]. Using the processing map, various defect generating cracking domains and regimes specifying manifestation of instabilities can be avoided during actual hot working. A brief account of the processing map theory is presented separately in the following section. In literature, a number of studies have appeared in regard to the optimization of hot workability of various complex alloys, e.g. powder metallurgy (P/M) superalloy Nimonic AP-1 [18], Zr-alloys [19], Titanium alloys [20], etc. Besides, few studies have recently appeared in literature illustrating the characterization of hot workability of few HEAs through the development of processing maps, such as CoCrFeMnNi HEA [21] CoCuFeNiMn HEA [22], and CoCuFeNiTi HEA [23] etc. Although, some authors [21–23] have reported hot workability of HEAs, none of them conducted an in-depth analysis in terms of microstructural correlation over each domain in the processing map constructed based on the DMM using a wide range of temperatures and strain rates.

Thus, the objectives of the present investigation are: (i) to characterize the hot working behavior of CoCrFeMnNi HEA *via* isothermal compression testing in the temperature range 1023 – 1423K and strain rate range 10^{-3} – $10s^{-1}$, (ii) to optimize the hot workability through construction of

processing map based on the principles of DMM, (iii) to characterize various deterministic domains and instability regime in a temperature – strain rate space in respect of operating deformation mechanisms and (iv) to identify 'safe' processing window for the alloy through avoidance of defects and manifestation of instabilities during hot working. Accordingly, an account of the hot workability characteristics of the CoCrFeMnNi HEA is presented in this paper through the construction of processing maps, illustrating various microstructural mechanisms operating in the deterministic domains and/or instability regimes. A suitable window in respect of temperature and strain rate ranges was established for safe processing of the HEA.

2. Theory of Processing Maps

In order to evaluate the hot workability characteristics of CoCrFeMnNi HEA, processing maps were constructed based on the principles of DMM, as proposed by Prasad et al. [17]. According to the theory of DMM, the instantaneous total power (P) dissipated at any instant comprises power dissipation through a temperature rise (G content) and a microstructural change (J co-content) and can be stated as a function of strain (ε), strain rate (ε′) and flow stress (σ) as described below:

$$P = \sigma.\dot{\varepsilon} = G + J = \int_0^{\sigma} \dot{\varepsilon}\, d\sigma + \int_0^{\dot{\varepsilon}} \sigma\, d\dot{\varepsilon} \quad (1)$$

The power partitioning between J co-content and G content is decided by the strain rate sensitivity of (m) of flow stress (σ) as follows:

$$\frac{dJ}{dG} = \frac{\dot{\varepsilon} d\sigma}{\sigma d\dot{\varepsilon}} = \frac{d(ln\sigma)}{d(ln\dot{\varepsilon})_{T,\varepsilon}} = m \quad (2)$$

At a given strain and temperature, the J co-content is given by:

$$J = \left(\sigma.\dot{\varepsilon}.\frac{\mathrm{m}}{\mathrm{m+1}}\right) \quad (3)$$

The J co-content of the workpiece, a nonlinear dissipator, is normalized with that of an ideal dissipator (m=1) to obtain a dimensionless parameter called the efficiency of power dissipation (η), expressed as:

$$\eta = \frac{J}{J_{max}} = \frac{2m}{m+1} \quad (4)$$

In simple terms, the efficiency describes the ability of the material to dissipate power through metallurgical processes. The variation of η as a function of $\dot{\varepsilon}$ and T at a given ε represents the constitutive behavior of the material and can be used to construct the power dissipation map [24]. A three-dimensional (3D) map of η plotted as a function of T and $\dot{\varepsilon}$ will have hills and valleys. A better presentation of power dissipation map is in the form of two-dimensional (2D) iso-efficiency contour map showing peak efficiency values in the center of the domains. Power dissipation maps generally comprise of deterministic domains (hills in 3D map) separated by bifurcation regimes (valleys in 3D map). The various domains in the map can be interpreted based on their peak efficiency values and can be correlated to the occurrence of specific microstructural processes.

In order to identify the regime of flow instabilities, the instability criteria developed by Prasad and Seshacharyulu [25] based on the continuum instability criterion by Ziegler et al. [26] is expressed as:

$$\xi(\dot{\varepsilon}) = \frac{\partial ln\left(\frac{m}{m+1}\right)}{\partial ln\dot{\varepsilon}} + m < 0 \quad (5)$$

The variation of the instability parameter $\xi(\dot{\varepsilon})$ with temperature and strain rates at constant strain is used to construct the instability map. The deformation region where, $\xi(\dot{\varepsilon}) < 0$ is predicted to be the regime for the occurrence of flow instabilities. This is the region where manifestation of instabilities in the form of adiabatic shear banding or flow localization may occur. The instability map may be superimposed on the power dissipation map to obtain a processing map, wherein the limits for the unstable flow regime are clearly demarcated. Moreover, microstructural characterization is needed to validate the deformation mechanisms associated with specific domains/regimes.

3. Experimental details

3.1 Material and Processing

The equiatomic CoCrFeMnNi HEA was drop-cast into a rectangular ingot (using 99.9% pure elemental powders) of approximately 140×40×40 mm^3. Melting of alloys was done using a vacuum arc melting furnace at KIMAB AB, Sweden. To enhance the chemical homogeneity, the drop-cast ingot was homogenized at 1423K for 12h in Ar-atmosphere followed by furnace cooling to room temperature. After homogenization, the alloy ingot was hot rolled at 1273K in several passes to a final thickness of 11mm. After each pass of the rolling, the alloy-ingot was kept inside the furnace and reheated to the rolling temperature. The cylindrical specimens of with the aspect ratio 1.24 (dimensions ~ϕ8×10mm) were machined from blanks extracted in the transverse-normal direction of the hot rolled sample.

Fig. 1 shows the schematic presentation of the uniaxial hot compression test schedules and processing conditions performed using a Gleeble® 3800 thermomechanical simulator. As illustrated, the specimens were first heated at 20K/s to 1423K and held for 5 min followed by cooling at 20K/s to the test temperature (1023 – 1423K). In order to even out the temperature, the specimens were held at the test temperature for 15s and then compressed to ~0.8 true strain by single-hit compression test at constant true strain rates (10^{-3}, 10^{-2}, 10^{-1}, 1 and $10s^{-1}$). The temperatures of samples were constantly monitored through the continuous feedback from the thermocouples that were spot-welded at the center of the samples, as shown in Fig. 1. In order to reduce the friction and barreling effect, the graphite foil was placed at the parallel surfaces of the test specimen as a lubricating agent. Additionally, thin tantalum foils were used to minimalize the temperature gradient and to prevent the specimens from gluing to the anvils, besides reducing the friction further. Finally, after the hot compression tests, the compressed air was used to fast cool the test specimens to the room temperature.

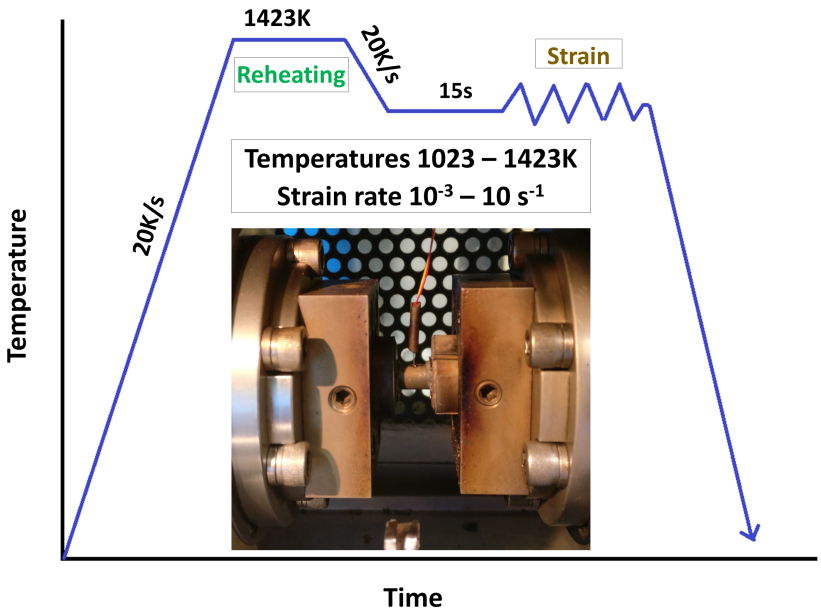

Fig. 1: A schematic diagram showing the experimental schedule and processing conditions for conducting hot compression tests in the Gleeble simulator.

3.2 Material characterization

For microstructural analysis, all the tested specimens were cut at mid-plane along the compression axis and then the samples were prepared for metallography through standard metallographic practices using conventional polishing techniques. This was followed by chemical etching using Kallings II reagent done over several steps, each extending over 2-5 seconds until a better view of the grain structure was revealed. The etching time varied in a narrow range for different samples in accord with variation in grain size, surface defects and etching response. The select samples were polished (using 0.02µm colloidal silica suspension) for the electron backscattering diffraction (EBSD) analysis.

The optical micrographs were recorded using a Leica DM 2500 optical microscope. Additionally, the chemical composition was analyzed using a Zeiss ULTRAplus field emission scanning electron microscope equipped with an X-MaxN 80 energy dispersive X-ray spectroscope (EDS) and Symmetry® (Oxford instruments) EBSD detector for the EBSD data acquisition. The EBSD data was acquired with a step size of 0.4µm at an acceleration voltage of 20kV and analyzed using the Channel 5 EBSD analysis software. The grain size was calculated with the minimum cut-off of a misorientation angle of 15˚ and only the grains above 10 pixels were considered to reduce the noise. Additionally, the grain boundaries were excluded from the grain size evaluations. A Matlab® 2019a programming platform was used to evaluate the hot compression data and an Origin® 2019b installation package was used to generate the plots.

A PAN analytic Empyrean Multipurpose Diffractometer is used to identify the phases of the samples by X-ray diffraction (XRD). The XRD data were collected at a step size of 0.013˚ in between 40-130˚ (2θ) with using the Co-K_α radiation as the characteristic X-ray beam for diffraction, operated at 40kV and 45mA.

4. Results

4.1 Initial microstructure

The chemical composition of the hot rolled HEA is shown in Table 1, obtained by averaging the measurements made by EDS at three different locations. Figs. 2a-c shows respectively, the optical micrograph, inverse pole figure (IPF) constructed using EBSD data and XRD peaks of the hot rolled sample. The average grain size calculated from EBSD map (Fig. 2b) was ~12.76 µm. The XRD peaks and EBSD analysis confirm the existence of FCC single phase material.

Table 1: Chemical composition of the CoCrFeMnNi HEA obtained by EDS analysis (at %.)

Co	Cr	Fe	Mn	Ni
20.1 ± 0.2	20.0 ± 0.1	20.0 ± 0.1	20.5± 0.4	19.5 ± 0.2

Furthermore, the EBSD components can evaluate the deformation level through measurement and calculation of the internal average misorientation angle within each grain. These details were analyzed by developing the recrystallization fraction maps using the HKL CHANNEL 5 software. To construct the recrystallization map, minimum misorientation angle criteria of 2˚ and 15˚ were applied in order to identify the subgrains and the grains, respectively. The grain was defined as a "deformed grain", if the average internal misorientation angle exceeded 2˚. If the grain contained subgrains whose average internal misorientation angles were under 2˚ and the misorientations between the subgrains were above 2˚, then the grain was classified as "sub-structured". The remaining grains are defined as "recrystallized" grains [27]. Thus, three different levels of deformation can be classified in the scanned grains, deformed, sub-structured (less deformed) and recrystallized.

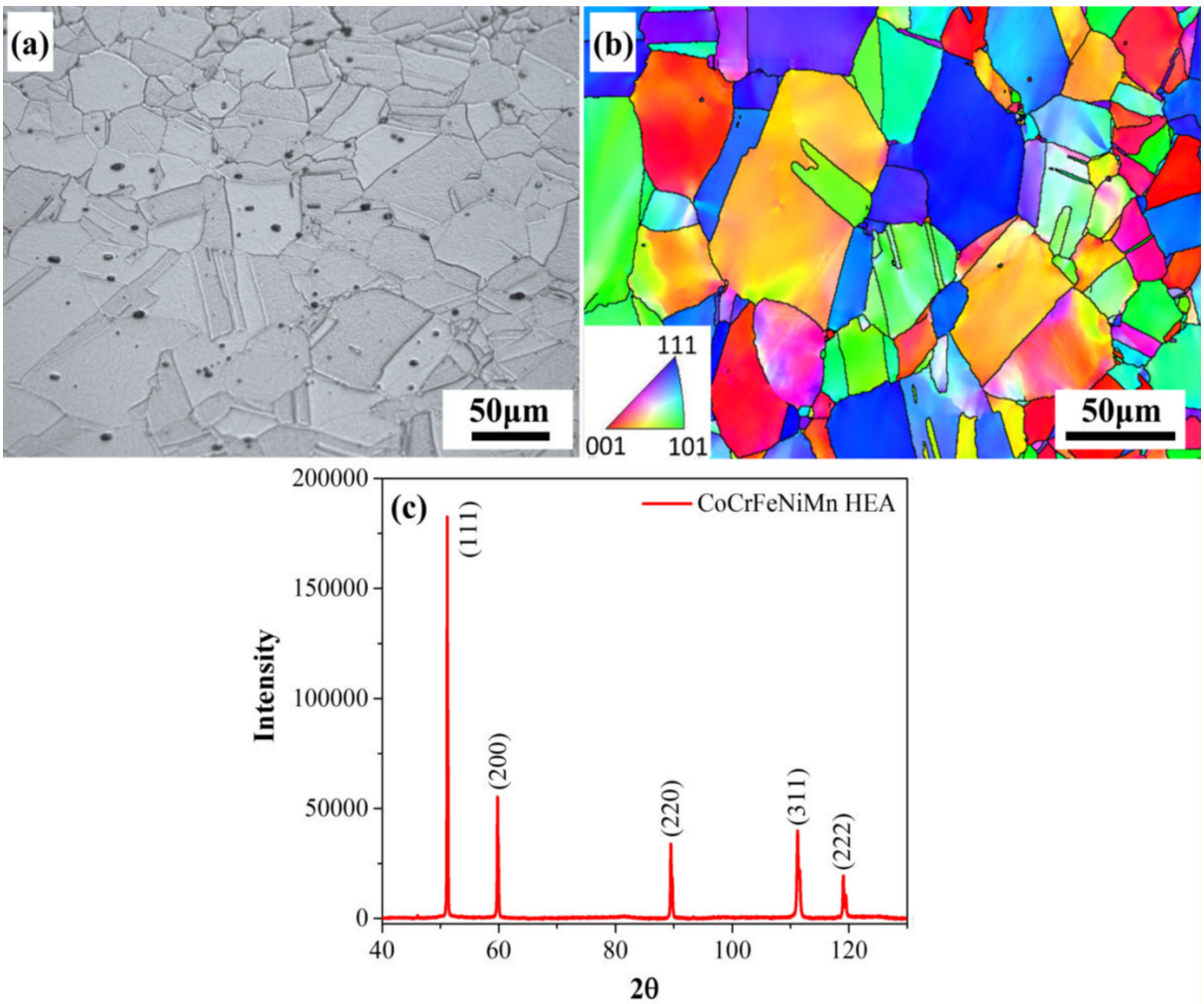

Fig. 2 (a) Optical Micrograph; (b) EBSD IPF map and (c) XRD data of the hot rolled CoCrFeMnNi HEA.

4.2 Flow stress behavior

The true strain vs. true stress curves obtained from the isothermal compression tests are shown in Figs. 3a-i. The flow stress values are strongly dependent on the deformation temperature, strain rate and strain. It can be seen that with the increase in strain rate and decrease in temperature, the flow stress increased significantly and the peak strain (ε_P) values shifted towards higher strains. At lower strain rates (10^{-3}, 10^{-2} and $10^{-1}s^{-1}$), irrespective of test temperatures the flow curves exhibited flow softening after showing the characteristic peak stress (σ_p) behavior. This σ_p followed by flow softening signify typical dynamic recrystallization (DRX) behavior, as explained by Eleti et al. [12].

At high strain rates (1 and $10s^{-1}$) and temperatures ≤1123K, the flow curves exhibited continuous work hardening behavior, i.e., the flow stress values increased with further straining. However, at temperatures ≥1173K, the flow stress values are nearly constant after reaching a maximum value and a nearly steady flow is maintained along the flow curves. This steady flow behavior is due to the dynamic balance between work hardening and dynamic recovery (DRV). Additionally, a decrease in work hardening rate or enhanced flow softening behavior is observed with increase in temperatures at high strain rates as shown in Fig. 3.

In the early stages of compression, the flow stress increases with increase in strain due to work hardening. The work hardening is caused by the generation of dislocations and their multiplication. The enhanced dislocation density leads to the formation of thick-walled subgrains, until the strain value surpasses the critical strain(ε_c). Eventually, at strains exceeding the ε_c values, the DRX process begins where new grains replace the original strained grains and the generation of DRX nuclei is assumed to be reliant on size of the substructured cell and the respective density of cell wall. In the flow curves normally the DRX is marked by flow softening behavior and steady-state flow on further straining. During further straining, the dynamic process of nucleation and migration of the newly formed strain-free grains is called DRX [27,28]. Additionally, the DRX is considered as the prime softening mechanism as the strain continuous. Also, the average DRX grain size is found to be constant and comprises the presence of substructure. This is attributed to presence of relatively high dislocation density due to continued deformation [28]. It should be noted that at low strain rates (≤ $10^{-1}s^{-1}$) the flow stress decreased reaching the σ_p during further straining.

Additionally, the flow softening behavior is known to occur due to the onset of flow instabilities and cracking as explained by Sellars et al. [14]. Thus, it is not quite appropriate to predict the microstructural evolution and deformation mechanism only based on the shape of the flow curves. The probable occurrence of dynamic restoration during hot deformation will be taken up in further detail through the microstructural analysis of the deformed samples.

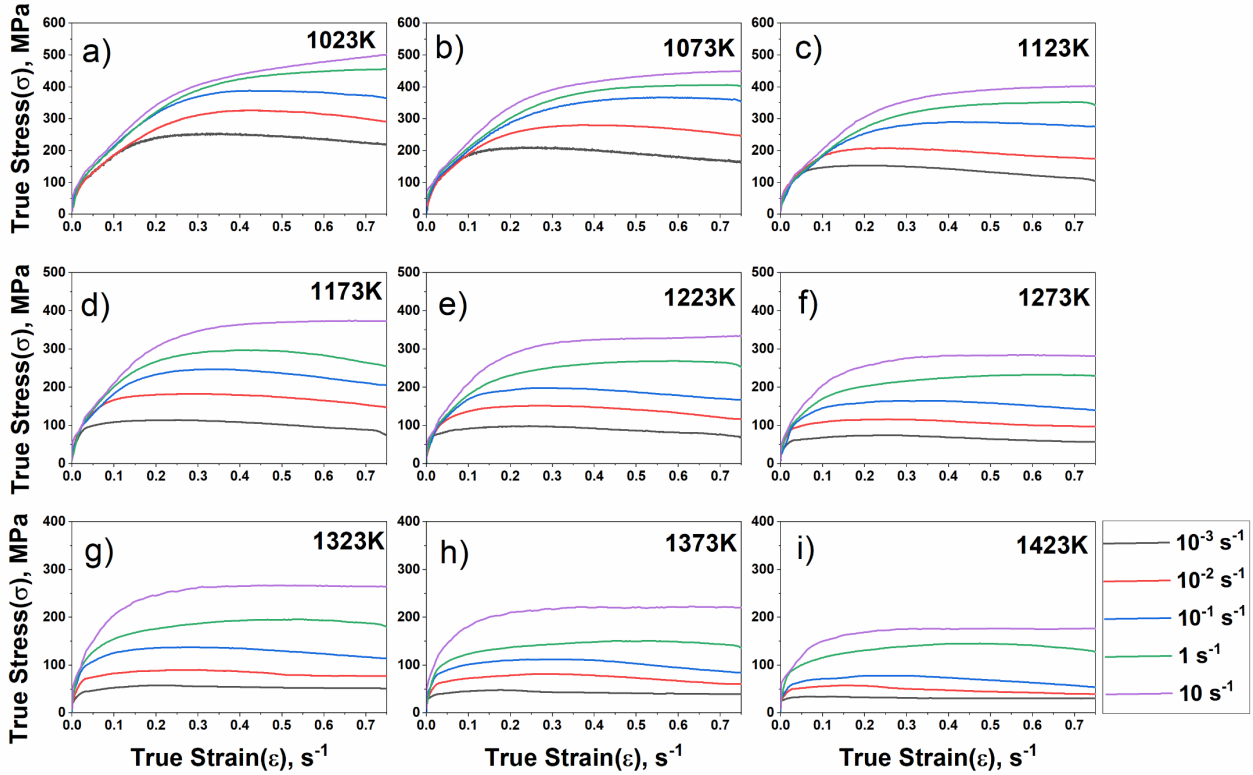

Fig. 3: True stress–true strain curve at the different strain rates at (a) 1023K (b) 1073K (c) 1123K (d) 1173K (e) 1223K (f) 1273K (g) 1323K (h) 1373K and (i) 1423K.

4.3 Calculation of η and $\xi(\dot{\varepsilon})$

To evaluate η at different strain rates ($\dot{\varepsilon}$) and temperatures (T) at a particular strain (ε), firstly the flow stress (σ) data at different $\dot{\varepsilon}$ and T were obtained from the true stress-strain curves. Further,

to compute the strain rate sensitivity (m) values, the experimental data were plotted as log (σ) vs. log $\dot{\varepsilon}$ at each temperature. These plots at each temperature were fitted with cubic splines as shown in Fig. 4 for a true strain of 0.6. According to Eq. (2), the first derivation of cubic spline was taken to calculate m values at small intervals of strain rates and temperatures. These m values were substituted into Eq. (4) to get the η values respectively. Additionally, the $\xi(\dot{\varepsilon})$ values were obtained in a similar manner by evaluating the slopes between $ln(m/m+1)$ vs $ln(\dot{\varepsilon})$ and adding the m-values.

The efficiency of power dissipation (η) was then calculated as a function of temperature and strain rate according to Eq. (4) corresponding to a true strain of 0.6 and plotted as a three-dimensional (3D) power dissipation map and a corresponding 2D iso-efficiency contour map. The data were also used to evaluate the instability parameter (ξ) according to Eq. (5) as a function of temperature and strain rate and to obtain an instability map. Accordingly, a 3D power dissipation efficiency (η) map was constructed for CoCrFeMnNi HEA over a temperature and strain rate ranges of 1023 – 1423K and 10^{-3} – $10s^{-1}$, respectively, at a true strain of 0.6, as shown in Fig. 5a. Fig. 5b shows the corresponding iso-efficiency contour map, which is easy to interpret the power dissipation map. Additionally, as per the criterion in Eq. (5), if the $\xi(\dot{\varepsilon})$ values are negative, the flow will be unstable. Thus, the region bounded by negative $\xi(\dot{\varepsilon})$ values plotted as a 3D instability (ξ) map in Fig. 5c suggests manifestation of instabilities causing unstable flow. Fig. 5d shows the corresponding two-dimensional instability map, which is easy to interpret and can be superimposed on the iso-efficiency contour map to give a processing map to delineate various deterministic domains and the regions of unstable flow, as shown in Fig. 6 for two different strains.

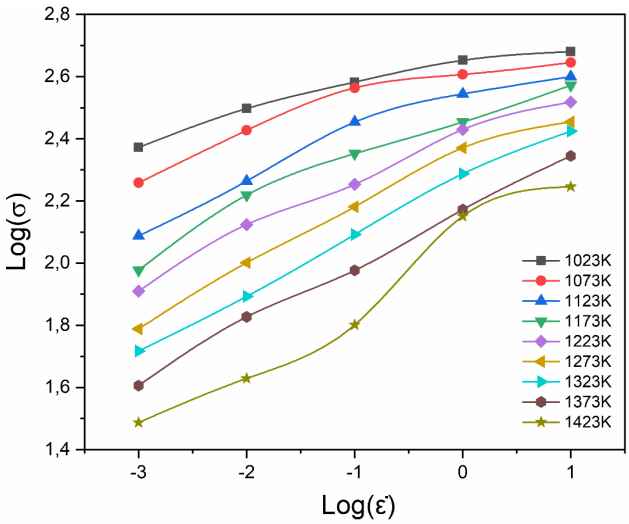

Fig. 4: Interpolation of log (σ) Vs log ($\dot{\varepsilon}$) at ε = 0.6 to evaluate m-values.

In order to understand the influence of different strains, the processing maps for CoCrFeMnNi HEA were constructed for two different strains, i.e., 0.5 and 0.6, as shown in Figs. 6a and b, respectively. The areas under the red colored contours that are superimposed over the power dissipation maps, are the instability regimes. In fact, the processing map at 0.6 strain in Fig. 6b is realized essentially through the superimposition of power dissipation and instability maps shown in Fig. 5b and 5d, respectively.

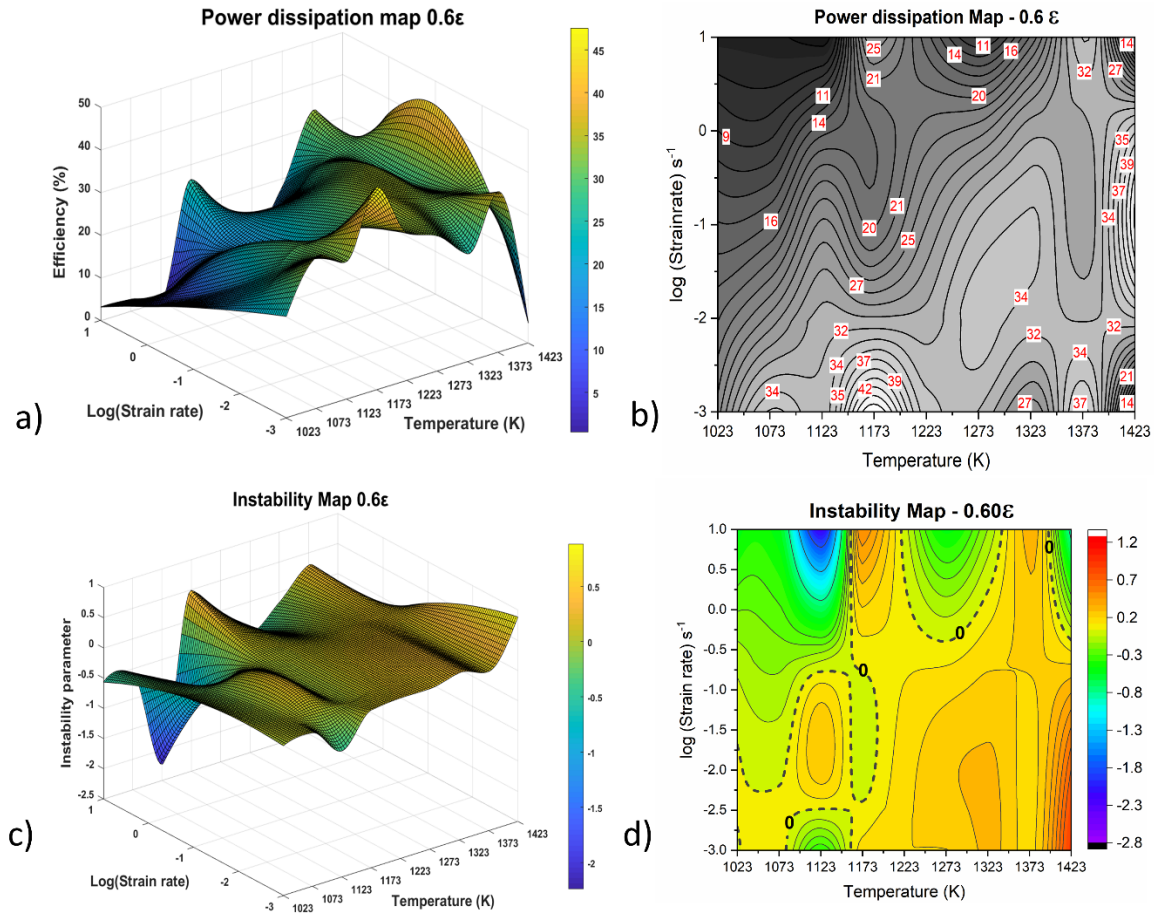

Fig. 5: (a) 3d power dissipation map, (b) Power dissipation contour map, (c) 3d instability map and (d) instability contour map of CoCrFeMnNi HEA at ε = 0.6.

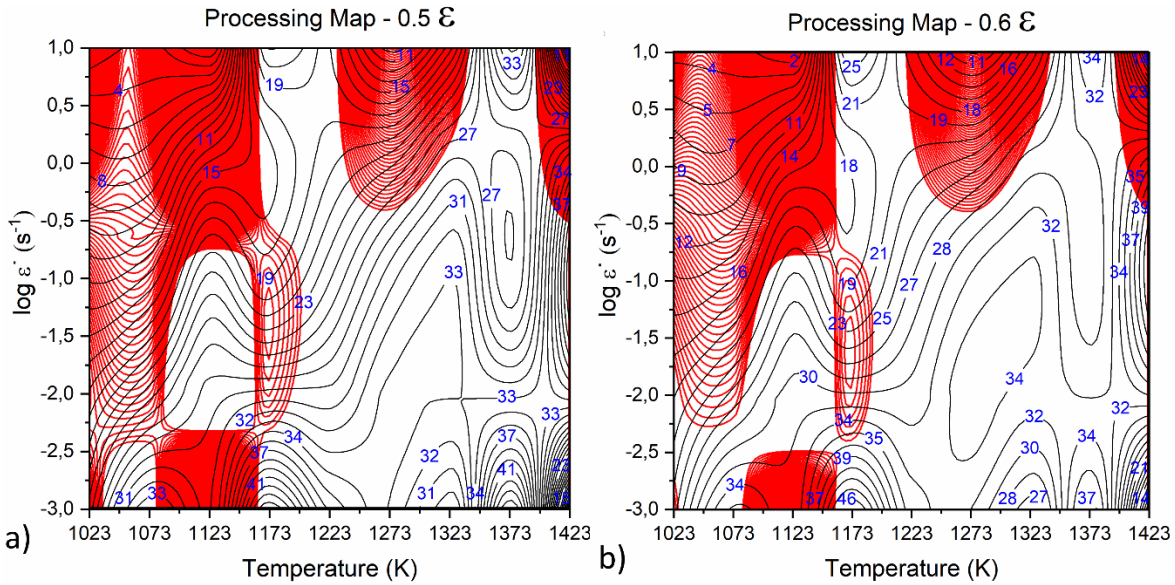

Fig. 6: Processing maps of CoCrFeMnNi HEA at strains ε = 0.5, and 0.6 where the region with red lines represents the instability zone.

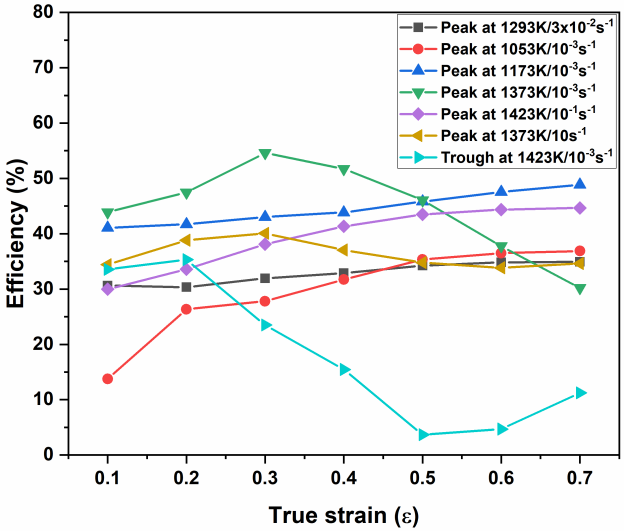

Fig. 7: Variation of peak (and trough) efficiencies with strain for various domains in the processing map at different strains.

The characteristics of the processing maps at other strains are almost similar when domains are concerned. However, the peak (and trough) efficiencies varied with increase in strain as shown in Fig. 7. The processing maps show 7 different domains:

1. A domain occurring at 1293K/3×$10^{-2}s^{-1}$ (domain B from Fig. 25) has a peak efficiency of 31 to 35 percent, increasing mildly with increasing strain. This domain spreads over a temperature range of 1223 – 1373K and strain rate in the range of 10^{-2} – 5×$10^{-1}s^{-1}$.
2. A domain occurring at 1053K/$10^{-3}s^{-1}$ (domain C from Fig. 25) has a peak efficiency in the range of 13 to 37 percent that is increasing steeply with strain.
3. A domain occurring at 1173K/$10^{-3}s^{-1}$ (domain D from Fig. 25) has a peak efficiency in the range of 41 to 49 percent that is increasing mildly with increasing strain.
4. A domain occurring at 1373K/$10^{-3}s^{-1}$ (domain E from Fig. 25) has peak efficiency varying from 44 to 30 percent. The efficiency initially increased to 54 percent somewhat steeply till 0.3 strain and then decreased to 30 percent till the 0.7 strain.
5. A domain occurring at 1423K/$10^{-1}s^{-1}$ (domain F from Fig. 25) has a peak efficiency increasing from 30 to 45 percent somewhat steep in the beginning up to 0.5 strain and then stayed practically flat.
6. A domain occurring at 1373K/10s^{-1} (domain H from Fig. 25) has peak efficiency increasing from 34 percent to 40 percent till 0.3 strain and then decreasing to 35 percent.
7. A domain occurring at 1423K/$10^{-3}s^{-1}$ (domain I from Fig. 25) has the trough efficiency which decreases from 33% to ~4% till 0.5 strain and then increases to ~11%. The domain has been characterized in respect of minimum efficiency that corresponds to the trough at the corner point in the map. There is a sharp decrease in iso-efficiency contours with the lowest efficiency analyzed at the corner, though the domain does not fall in the instability regime, see Fig. 6a,b.

5. Discussion

5.1 Interpretation of Processing Maps

Each deterministic domain in the processing map is interpreted in respect of its efficiency of power dissipation and verified in terms of microstructural evolution to validate the predictions of the processing maps. Likewise, the instability regimes are interpreted and verified in respect of manifestation of instabilities. For instance, manifestation of instability features such as adiabatic shear bands, flow localization, voids, etc. are carefully identified in the regions of unstable flow. On the other hand, the efficiency of power dissipation by cracking processes is generally high, since the energy conversion into surface energy is very efficient. Restoration processes like DRX are relatively

less efficient processes and are marked by nearly similar peak efficiencies of power dissipation over a large strain. While the adiabatic shear band formation are likely to form at high strain rates, instabilities manifesting as voids or cracks along intense bands occur at low temperatures and high strain rates [18]. Additionally, at high temperature and lower strain rates wedge cracking is expected to form at the triple junction of the grain boundaries. These regions, therefore, are not safe for hot working. In contrast, temperature and strain rate ranges typical of DRX (high temperatures and strain rates) and DRV (low temperatures and strain rates) behaviors are known as safe working domains.

5.1.1 Domain at 1293K and 3×10^{-3} s^{-1}

This domain extends over a temperature range of 1223 – 1373K and strain rates in the range 10^{-2} – $5\times10^{-1}s^{-1}$. The optical micrographs of the specimens deformed at 1223K, 1273K and 1323K at $10^{-2}s^{-1}$ and; 1273K and 1323K at $10^{-1}s^{-1}$ are shown in Fig. 8a-e, respectively. When compared to the microstructure of as-hot rolled specimen, the grain size seems finer. The samples tested in this region did not show any signs of instabilities or cracking. Fig. 7 also indicated that the peak efficiency of power dissipation in this domain was relatively uniform over the imposed strain. The microstructures in Fig. 8a-c exhibit fine DRX grains, with the recrystallized grain size increasing with increasing temperature and decreasing strain rate. Nucleation of fine DRX grains was observed at prior grain boundaries, which further grew inhomogeneously with increasing temperature. Further, it can be noticed from Fig. 8d-e that the recrystallized fraction gradually decreased as the strain rate increased, whereby most grains appear somewhat elongated and may contain substructures.

Additionally, from Figs. 3e-g it is observed that the flow stress decreased after the peak stress (σ_p) at all testing conditions consistent with the microstructures presented in Figs. 8a-e. The σ_p behavior showing the softening of flow stress also justifies the occurrence of DRX. Eleti et al. [12] reported formation of DRX grains along the grain boundaries in CoCrFeMnNi HEA besides annealing twins under similar testing conditions, and the volume fraction of DRX grains increased with the increase in temperature and decrease in strain rate. Huang et al. [29] and Zaddach et al [30] reported that CoCrFeMnNi HEA was a low stacking fault energy (SFE) material at room temperature. However, according to the *abinito* calculations by Huang et al. [29], increase in temperature increased the SFE values. Additionally, Mirzadeh et al. [31] demonstrated that low SFE materials undergoing deformation showed annealing twins, which played an important role in nucleation and growth of DRX grains during hot deformation. Also, in the present study, the EBSD maps reveal the formation of annealing twins within the DRX grains. Figs. 9a,c and 9b,d shows the band contrast images and recrystallization fraction maps of the specimens deformed at 1273K/$0.1s^{-1}$ and 1323K/$0.1s^{-1}$ respectively. The red colored grain boundaries in band contrast images are Σ3 twin boundaries with misorientation angle of 60° (maximum deviation ~5°). The black colored grain boundaries are high angle grain boundaries (HAGBs) with misorientation angles greater than 15°. It is clearly visible in Figs. 9a,c that the twin boundaries formed all along in the DRX grains, which nucleated along the prior grain boundaries. Additionally, the recrystallization maps show that the recrystallization fraction (blue colored grains) without substructure decreased from 16.9% to 11% with the increase in temperature. Further to this, the band contrast images show that the twin boundaries decreased from 6.33% to 3%. The increase in temperature resulted in the growth of the DRX grains, which did simultaneously undergo deformation during continued straining thus leading to the occurrence of substructures. The grain boundary misorientation too changed continuously during the growth of the former DRX grains (yellow colored), which were substructured due to the continued deformation.

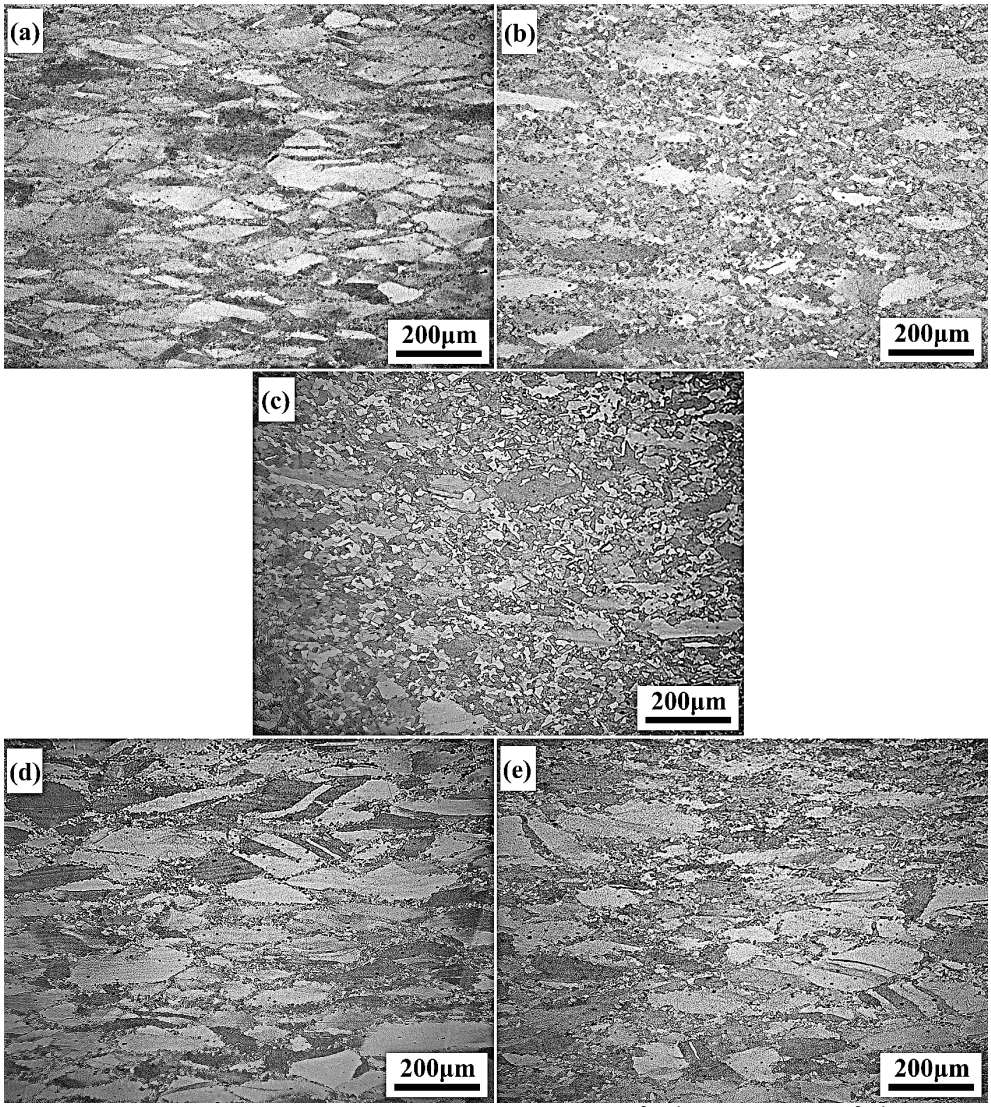

Fig. 8: Micrographs of CoCrFeMnNi HEA deformed at; (a) 1223K/10^{-2} s^{-1}; (b) 1273K/$10^{-2}s^{-1}$; (c) 1323K/$10^{-2}s^{-1}$; (d) 1273K/$10^{-1}s^{-1}$; (e) 1323K/$10^{-1}s^{-1}$.

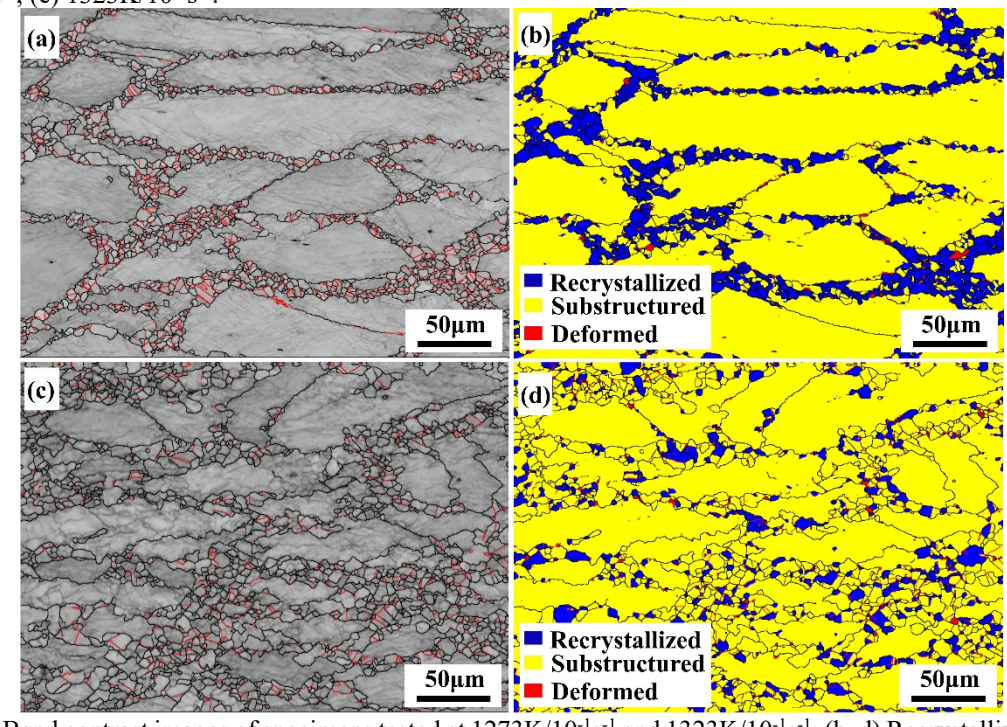

Fig. 9: (a, c) Band contrast images of specimens tested at 1273K/$10^{-1}s^{-1}$ and 1323K/$10^{-1}s^{-1}$; (b, d) Recrystallization fraction images of specimens tested at 1273K/$10^{-1}s^{-1}$ and 1323K/$10^{-1}s^{-1}$.

5.1.2 Domain at 1053K/10^{-3} s^{-1}

This is a small domain extending over 1023K-1098K and strain rates in the range 10^{-3} – $3\times10^{-3}s^{-1}$. The optical micrographs of the specimens deformed at 1023K/$10^{-3}s^{-1}$ and 1073K/$10^{-3}s^{-1}$ are shown in Figs. 10a,b. The micrographs show necklace-type structure with fine, equiaxed grains at the grain boundaries of the elongated grains. Additionally, grain boundary cracking/sliding is visible near the grain boundaries as marked with arrows in Figs. 10 a,b. This GB cracking/sliding can occur during deformation at low temperatures and low strain rates [32]. Figs. 3a,b shows the occurrence of flow stress softening with increase in strain beyond the σ_p both at 1023K and 1073K deformed at 10^{-3} s^{-1}. The flow softening behavior corroborates the initiation of strain-free new DRX grain formation along the grain boundaries. However, the dislocations were not distributed uniformly at this low temperature due to slower dislocation motion. Thus, the dislocations accumulated at grain boundaries at a lower strain rate ($10^{-3}s^{-1}$) facilitated the occurrence of grain boundary cracking. With an increase in testing temperature beyond 1073K (Fig. 10b), the grain boundary cracking tendency was significantly reduced. Eleti et al. [12] performed hot compression testing of CoCrFeMnNi HEA at different temperatures and reported that the flow softening did occur at 1073K/$10^{-3}s^{-1}$, but with the formation of more equiaxed grains along the grain boundaries in contrast to our results, even though the strains in their tests were only marginally higher (0.9 strain) compared to the present work (about 0.8 strain).

Also, the efficiency of power dissipation in this domain increases steeply with the increase in strain from 13% to 37%, Fig. 7. Thus, this domain is not safe for hot working, as inferred from the predictions of the processing map and verified through microstructural analysis.

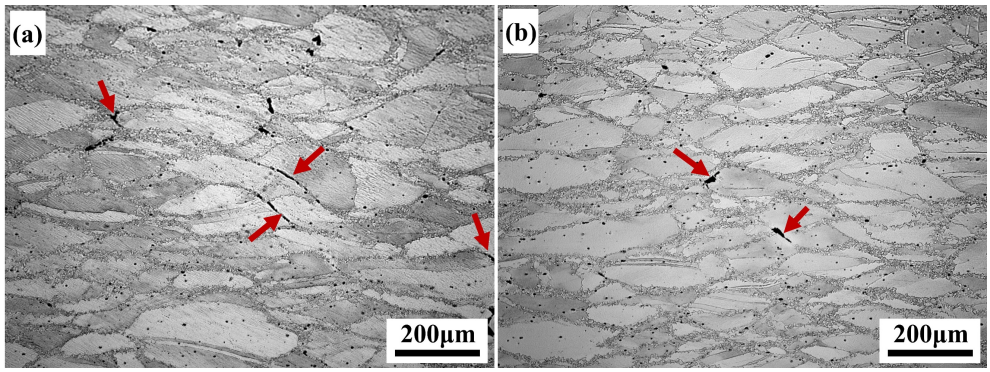

Fig. 10: Micrographs of CoCrFeMnNi HEA deformed at; a) 1023K / 10^{-3} s^{-1}; b) 1073K / $10^{-3}s^{-1}$.

5.1.3 Domain occurring at 1173K/$10^{-3}s^{-1}$

This domain extends over 1123K to 1223K over a narrow strain rate range of 10^{-3} to $3\times10^{-3}s^{-1}$. The optical micrographs of the specimens deformed at $10^{-3}s^{-1}$ at different temperatures are shown in Figs. 11a-c. The flow stress at the deformation conditions 1123K/$10^{-3}s^{-1}$ and 1223K/$10^{-3}s^{-1}$ decreased with increase in strain (Figs. 3c,e), however at 1223K/$10^{-3}s^{-1}$, the flow curve showed slight softening beyond the peak stress (σ_p) followed by nearly steady-state behavior with strain. The micrographs show DRX grains along the grain boundaries of elongated grains (Fig. 11a-c). The increase in temperature led to an increase in the volume fraction of recrystallized grains and also, the grain size. Eleti et al. [12] also showed that the deformation of CoCrFeMnNi HEA at 1173K/$10^{-3}s^{-1}$ exhibited large DRX grains as compared to that formed at 1073K/$10^{-3}s^{-1}$. Additionally, from Figs. 11a,b the presence of shear bands can clearly be seen within the region as marked by dotted lines. The EBSD analysis of 1173K/$10^{-3}s^{-1}$ sample (Fig. 12b) shows the presence of recrystallized grains (blue colored, about 17.9% volume fraction) with ~9.5% twin boundaries (∑3) (Fig. 12a), suggesting the formation of twins alongside the DRX process or subsequent growth. As shown in Fig. 12b, the fraction of highly deformed grains (red colored grains) is only ~1.3%, which means that shear bands formed due to the shear localization as a case of geometrical softening i.e. during the deformation, the structure oriented itself to the direction that was easier for its glide [33].

An increase in the deformation temperature reduced the possibility of localized shear band formation, as is evident in Fig. 11c, which does not present clear evidence of flow localization or shear/ deformation bands. Additionally, the peak efficiency of power dissipation in this domain increased mildly from 41 to 49% with the increase in strain as shown in Fig. 7. Based on the microstructural observations, the domain is not safe for hot working due to the formation of localized shear bands, corroborating the mild increase in peak efficiency value with strain.

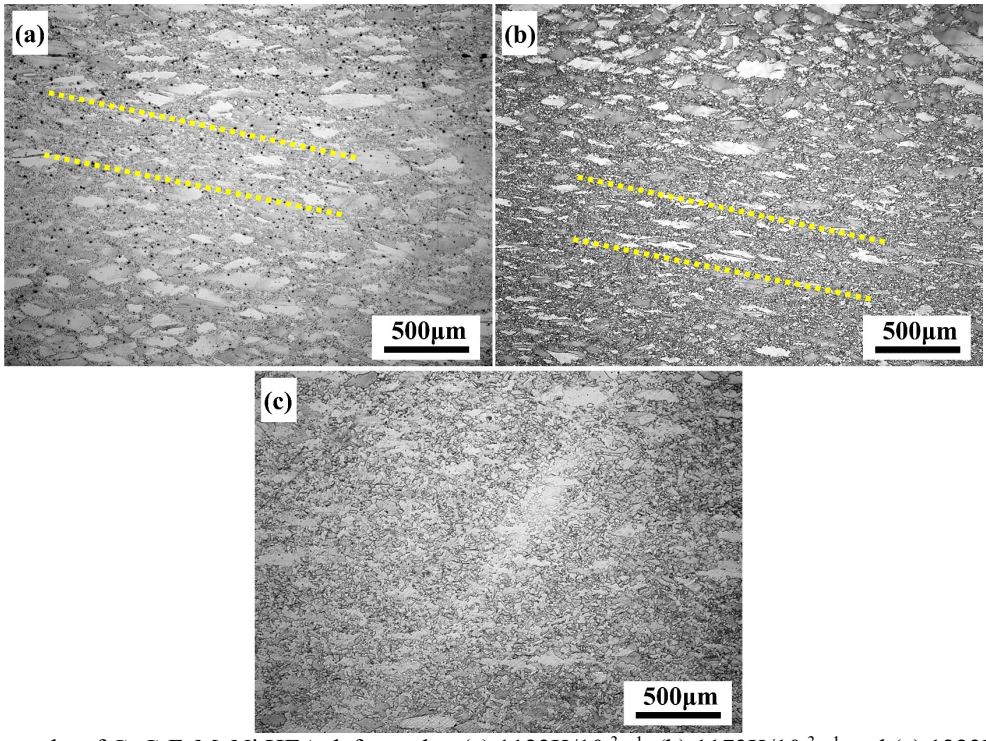

Fig. 11: Micrographs of CoCrFeMnNi HEA deformed at (a) 1123K/$10^{-3}s^{-1}$, (b) 1173K/$10^{-3}s^{-1}$ and (c) 1223K/$10^{-3}s^{-1}$.

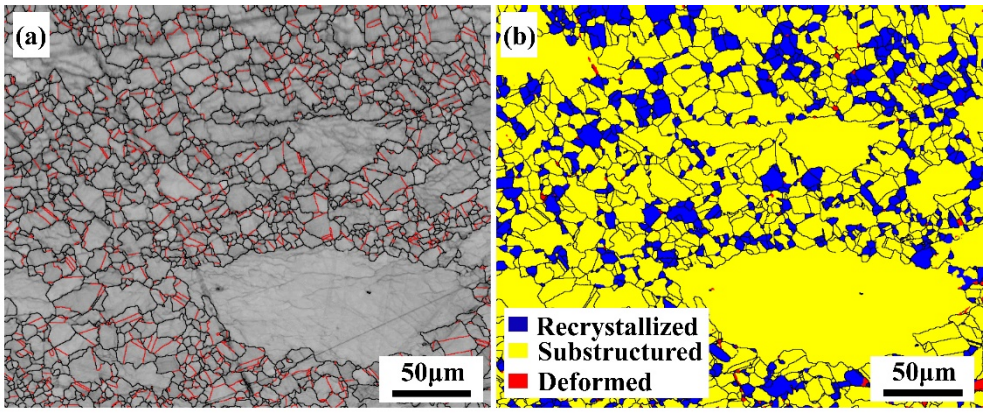

Fig. 12: (a) Band contrast image and (b) recrystallization fraction map of CoCrFeMnNi HEA deformed at 1173K/$10^{-3}s^{-1}$.

5.1.4 Domain at 1373K/$10^{-3}s^{-1}$

This domain extends in a short range from 1348 – 1403K and strain rates in the range $10^{-3}s^{-1}$ – $3\times10^{-3}s^{-1}$. The light optical micrograph of the sample deformed at 1373K/$10^{-3}s^{-1}$ is shown in Fig. 13, which clearly exhibits relatively large equiaxed recrystallized grain structure. Normally at high temperature and low strain rate conditions, the dislocations are largely absorbed in subgrain boundaries, thus increasing the misorientation and leading to the formation of HAGBs through subgrain rotation and coalescence (continuous recrystallization). The reason for rotation and grain growth at this elevated temperature is due to the occurrence of both the dislocation glide and climb [34]. The flow stress at 1373K/$10^{-3}s^{-1}$, as shown in Fig. 3g, exhibits a steady-state behavior after reaching the peak, which corresponds to the grain growth of the DRX grains.

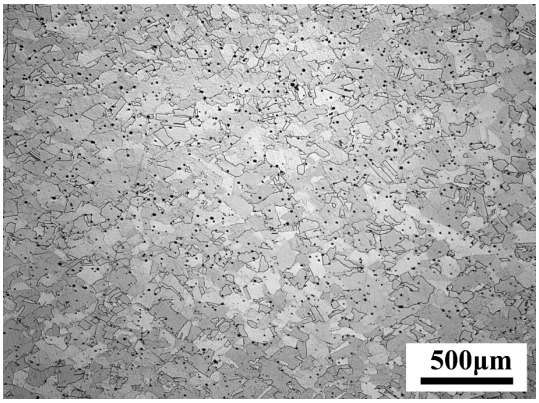

Fig. 13: Micrographs of CoCrFeMnNi HEA deformed at 1373K/$10^{-3}s^{-1}$.

In this domain due to excessive grain boundary sliding, there are increased chances of the occurrence of wedge cracking, as explained by Somani et al. [18]. As such, no wedge crack could be detected in the microstructure, but the power dissipation peak efficiency is quite high and crossed 50% at 0.3 and 0.4 strains as shown in Fig. 7, normally associated with superplastic behavior that coincides with wedge cracking [32]. The domain is, therefore, not stable/safe for hot working.

5.1.5 Domain at 1423K/$10^{-3}s^{-1}$

This domain extends in a short range from 1403 – 1423K and strain rates in the range $10^{-3}s^{-1}$ – $3\times10^{-3}s^{-1}$. This domain shows sharply decreasing iso-efficiency contours with very low efficiency at the corner. The microstructure of the concerned sample is shown in Fig. 14, which did not reveal any cavitation or formation of wedge cracks occurring under such conditions. However, there is extensive grain growth, masking any information regarding the possibility of subgrain coalescence that might have taken place, similarly as in the neighboring domain at 1373K/$10^{-3}s^{-1}$. In any case, this domain is not desirable for processing due to its sharply decreasing efficiency, grain coarsening and moreover, the likelihood of wedge cracking.

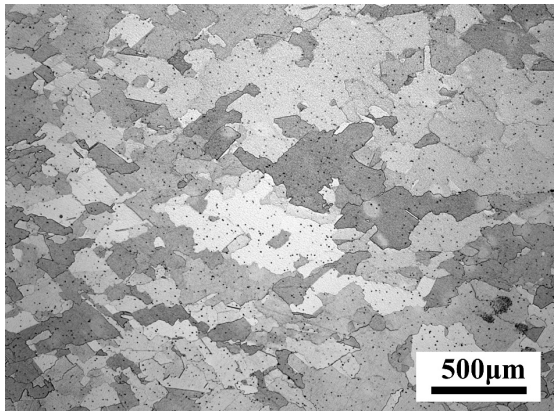

Fig. 14: Micrographs of CoCrFeMnNi HEA deformed at 1423K/$10^{-3}s^{-1}$.

5.1.6 Domain occurring at 1423K/$10^{-1}s^{-1}$

This domain extends from temperature in the range 1398 – 1423K and strain rate in the range 10^{-2} – $3\times10^{-1}s^{-1}$.The shape of the flow stress curves at 1423K/$10^{-1}s^{-1}$ (Fig. 3i) seems unusual in the beginning till 0.3 strain which is also reflected in its sharp increase in peak efficiency values with strain (Fig. 7), followed by more stable flow akin to DRX and grain growth that is reflected in the peak efficiency of this domain (~44%). Additionally, in this domain, the efficiency increased steeply with increase in temperature, as seen from relatively close contours in Fig. 6b. These features indicate an increase in chances of occurrence of intercrystalline cracks, as explained by Somani et al. [18]. Since the microstructures as shown in Figs. 15a-b are recorded at room temperature following fast cooling to room temperature, and shows no sign of intercrystalline cracks or any type of fracture. However, the grain growth can be seen in Fig. 15. Thus, it is difficult to assume whether any unstable flow occurred

during hot deformation. In any case, this domain is not desirable for processing due to steep increase in efficiency and the likelihood of fracture.

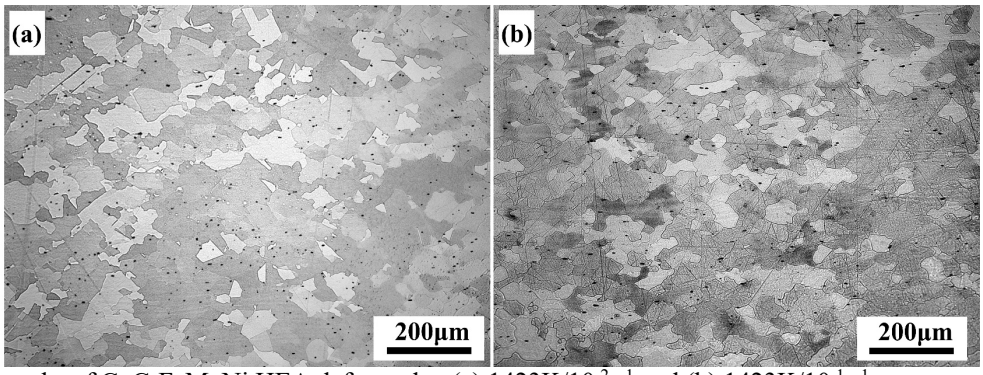

Fig.15: Micrographs of CoCrFeMnNi HEA deformed at (a) 1423K/$10^{-2}s^{-1}$ and (b) 1423K/$10^{-1}s^{-1}$.

5.1.7. Domain occurring at 1373K/$10s^{-1}$

This domain extends from 1348 – 1398K in the strain rate range 3 – $10s^{-1}$. The micrograph of the sample deformed at 1373K/$10s^{-1}$ is displayed in Fig. 16. The micrograph shows recrystallization along with few elongated grains. The peak efficiency of power dissipation in this domain increases initially till 0.3 strain from 34% to 40% and eventually decreases to ~34% at 0.7 strain as shown in Fig. 7. The flow curve at this test condition remained flat (steady-state) with increase in strain after reaching the peak value. This type of flow curve predicts continuous recrystallization behavior. Additionally, the band contrast image recorded during the EBSD study, as shown in Fig. 17a, showed a higher percentage of twin boundaries (33.4%), which confirms continuous recrystallization inside the recrystallized grains. The recrystallization fraction as shown in Fig. 17b is 82.8%. This shows the occurrence of continuous recrystallization and is possible at high temperatures and high strain rates, as also explained by Humphreys et al. [35]. Hot working in this domain could be potential raise the production rates without any occurrence of microstructural defects. However, to confirm the potential safe working conditions there should be more tests conducted in this region with strain rates from 3 – $10s^{-1}$ as this domain looks very small because the Figs. 6a,b are represented in logarithmic scale.

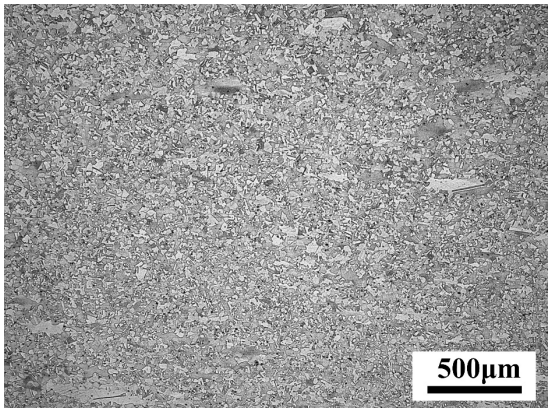

Fig. 16: Micrographs of CoCrFeMnNi HEA deformed at 1373K/$10s^{-1}$.

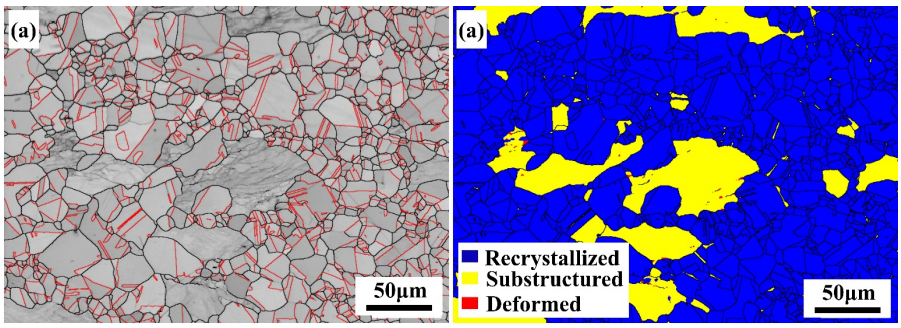

Fig. 17: (a) Band contrast images and (b) recrystallization fraction image of CoCrFeMnNi HEA deformed at 1373K/$10s^{-1}$.

5.2. Manifestation of instability

Flow instability is anticipated to arise when the value of $\xi(\dot{\varepsilon})$ turns negative. The red colored regions as indicated within the processing maps (Figs. 6a,b) correspond to the instability regimes. Deformation within the instability regime may exhibit manifestation of various defects, such as flow localization, adiabatic shear bands, grain boundary crack etc. [36]. To validate the regions of unstable flow, detailed microstructural analysis of select samples corresponding to the instability regime have been carried out. It can be seen that the temperature range of the instability domain increased with the increase in strain rate. This might be due to lesser time available for dislocation motion or distribution for avoidance of defect formation. In the following section, details of the features noticed in the instability regime are discussed at 5 different strain rates.

5.2.1 Instability at $10^{-3}s^{-1}$

The microstructural features of the instability regions at 10^{-3} s^{-1} have previously been discussed in section 5.1.2 and section 5.1.3. The unstable domain at this strain rate extends over 1023 – 1173K. At low temperatures (between 1023 – 1098K) the micrographs (Figs. 10a, b) show the presence of GB cracking or sliding. At the temperatures between 1123 – 1173K, the micrographs (Figs. 11a, b) show the formation of shear bands due to geometric softening caused by shear localization. At high temperatures (1403 – 1423K) as explained in section 5.1.5 showed sharp decrease in efficiency and grain coarsening and likelihood of wedge cracking.

5.2.2 Instability at $10^{-2}s^{-1}$

The optical micrographs of specimens deformed at $10^{-2}s^{-1}$ at different temperatures (1023K, 1073K, 1123K and 1173K) are shown in Figs. 18a-d, which clearly bring out the occurrence of grain boundary cracking (marked with red arrows), voids and shear bands. With the increase in temperature, the tendency to grain boundary cracking decreased. Even though the test condition 1123K/$10^{-2}s^{-1}$ doesn't fall in the instability regime (according to Fig. 6), the presence of shear bands and grain boundary cracks noticed in the deformed sample identifies that this test condition too is unsafe for hot working.

The flow stress curves at respective test conditions, as shown in Figs. 3a-d, show softening of flow stress with strain beyond the peak stress (σ_p), and very fine grains can be seen nucleating at the grain boundaries as shown in Figs. 18c,d, whose number and volume increased with the increase in temperature as enough time was available for dislocation redistribution and tendency to reduced grain boundary cracking.

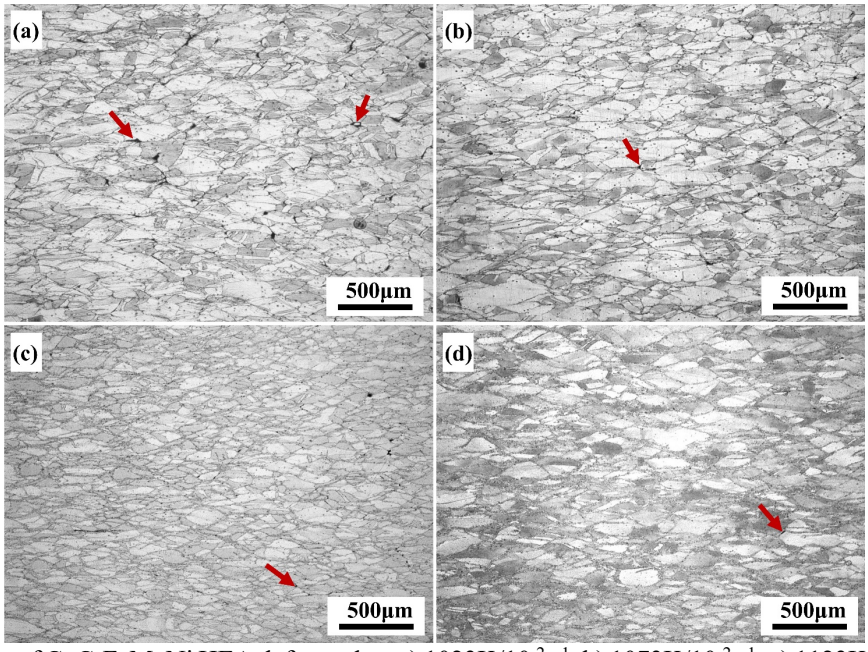

Fig. 18: Micrographs of CoCrFeMnNi HEA deformed at; a) 1023K/$10^{-2}s^{-1}$; b) 1073K/$10^{-2}s^{-1}$; c) 1123K/$10^{-2}s^{-1}$; d) 1173/$10^{-2}s^{-1}$.

5.2.3 Instability at $10^{-1}s^{-1}$

Fig. 19a-d show the micrographs of specimens tested at 1023 – 1173K at $10^{-1}s^{-1}$. All the micrographs exhibit formation of voids along the grain boundaries, marked by arrows. The flow stress curves at the respective test conditions, as shown in Figs. 3a-d, show softening behavior beyond the σ_p. However, at 1073K/$10^{-1}s^{-1}$, the flow stress curve shows strain hardening behavior. Fig. 19b clearly reveals the occurrence of voids and cracks along the grain boundaries. The propensity to void/crack formation decreased with the increase in temperature. In effect, the dislocation motion increases with temperature and then at 1173K/$10^{-1}s^{-1}$, it is clear that fine grains formed along the grain boundaries (as shown in Fig. 19d along the dotted lines). There are hardly any signs of restoration processes visible in Figs. 19a-c. Additionally, all the images show the presence of shear bands as shown in the regions between the dotted lines, which are due to flow localization. Though the region surrounding the test condition 1123K/$10^{-1}s^{-1}$, as shown in Fig. 6, does not fall under the instability regime, the corresponding micrograph, as shown in Fig. 19c, comprised of voids and shear bands. Thus, this region, too, is not safe for hot working.

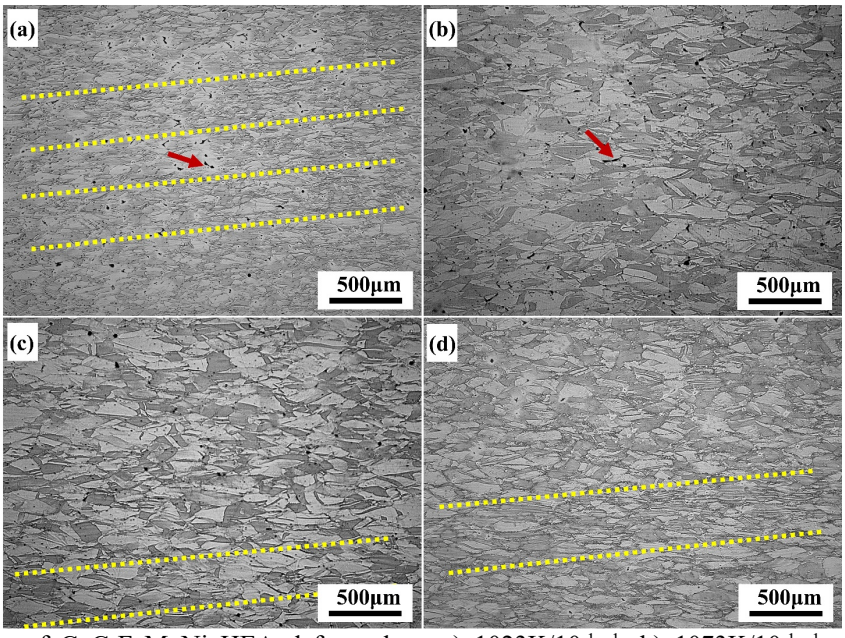

Fig. 19: Micrographs of CoCrFeMnNi HEA deformed at; a) 1023K/$10^{-1}s^{-1}$; b) 1073K/$10^{-1}s^{-1}$; c) 1123K/$10^{-1}s^{-1}$; d) 1173K/$10^{-1}s^{-1}$.

5.2.4 Instability at $1s^{-1}$

The instability regime at $1s^{-1}$ strain rate extends from 1023 – 1273K temperatures as shown in Fig. 20. The corresponding micrographs depicted in Figs. 20 a-f clearly reveal formation of adiabatic shear bands, as marked by areas inside the yellow dotted lines. The corresponding flow curves at 1023 – 1123K (Figs. 3a-c) confirm that the flow stress increased with the increase in strain displaying work hardening behavior. The voids or cracks along the grain boundaries are clearly visible (shown with red arrows). Deformation at a high strain rate and lower temperature restricts the dislocation motion due to shorter duration of deformation. Thus, the accumulated dislocation density can lead to grain boundary cracking. Also, at higher strain rates, work hardening results in dissipation of viscoplastic heat in addition to the occurrence of microstructural changes (grain distortion, glide, dislocation motion). If the heat generated doesn't have enough time to escape along the deformation area, this may lead to localized temperature rise and formation of thin bands [33]. These bands are known as adiabatic shear bands. The EBSD measurements at 1023K confirmed the formation of adiabatic shear bands under these deformation conditions, i. e., the deformation fraction is ~42.5%, as shown in Fig. 21b (red color grains). This confirms that the specimen is highly deformed, and this plastic deformation led to the heat generation which resulted in adiabatic shear bands.

Further increase in deformation temperature resulted in flow softening and steady-state behavior beyond the σ_p as a function of strain. The heat generated due to deformation and the higher

temperature of testing provided enough driving force for the nucleation of new DRX grains along the grain boundaries or in the shear bands, thus alleviating the microstructural inhomogeneity. Figs. 21c,d show the same, i.e., the percent twins (red colored) as shown in Fig. 21c increased alongside the recrystallization fraction (blue grains) as shown in Fig. 21d. However, the presence of shear bands (flow localization) renders this temperature unsuitable for hot working.

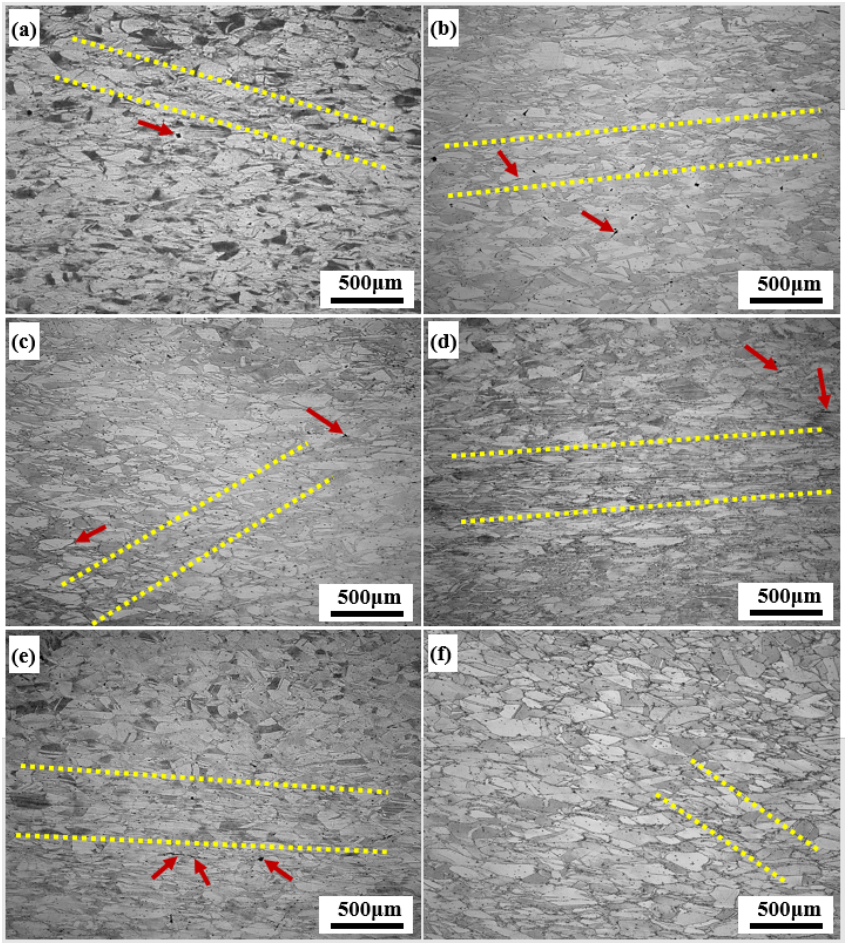

Fig. 20: Micrographs of CoCrFeMnNi HEA deformed at; a) 1023K/1s^{-1}; b) 1073K/1s^{-1}; c) 1123K/1s^{-1}; d) 1173K/1s^{-1}; e) 1223K/1s^{-1}; f) 1273K/1s^{-1}.

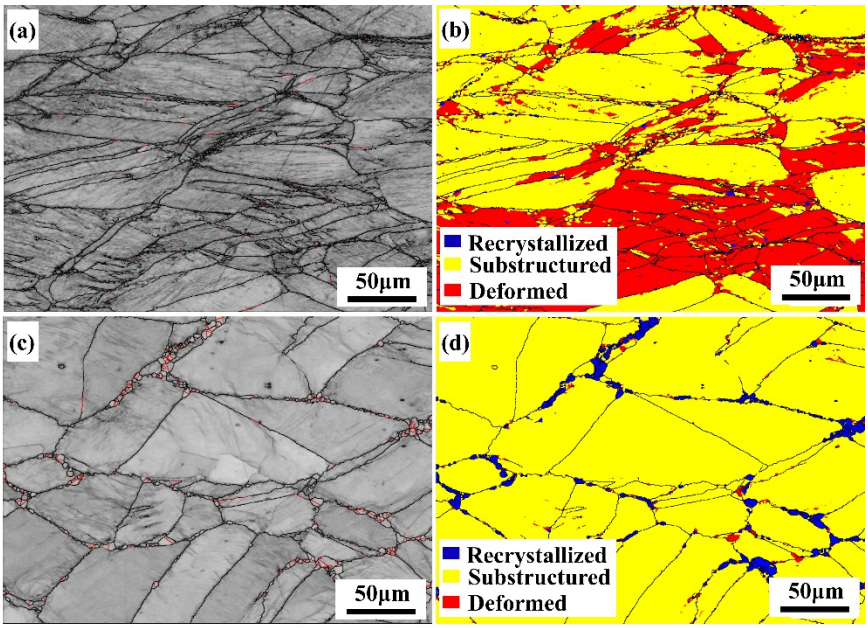

Fig. 21: (a), (c) Band contrast images of specimens tested at 1023K/1s^{-1} and 1273K/1s^{-1}; (b), (d) Recrystallization fraction images of specimens tested at 1023K/1s^{-1} and 1273K/1s^{-1}.

5.2.5 Instability at $10s^{-1}$

The instability regime at the high strain rate $10s^{-1}$ is comprised of the entire test temperature range, except at $1373K/10s^{-1}$, as shown in Fig. 6. The microstructures recorded at various temperatures are shown in Figs. 22a-g, which confirm the presence of instabilities i.e. adiabatic shear bands, cracks and voids. The flow curves at temperatures $1023 – 1123K/10s^{-1}$, as presented in Figs. 3a-f, indicated continuous strain hardening over the strain range obviously as a result of high strain rate. Thus, due to work hardening, a number of microstructural defects were generated in the structure. It is apparent in Figs. 22a-e that the micrographs are comprised of shear bands (areas marked by the dotted lines) due to flow localization. At the high strain rate ($10s^{-1}$), adiabatic shear bands formed due to excessive heat generation in a very short duration and lack of time for heat dissipation during the deformation. Figs. 22a,b show respectively, the band contrast image and the recrystallization fraction map, recorded on the sample tested at $1123K/10s^{-1}$. The recrystallization fraction map displays that the fraction of highly deformed grains (red colored) is relatively high (~28.9%) with only a small fraction of recrystallized grains (~2.5%). The highly deformed grains are localized. Additionally, the band contrast image (Fig. 22a) shows that there is only a small fraction (~0.4%) of twin boundaries ($\sum 3$).

Figs. 3f,g shows the flow curves of samples tested at $1273K/10s^{-1}$ and $1323K/10s^{-1}$. The flow curves are essentially flat exhibiting steady-state behavior at these conditions. Additionally, the micrographs of these samples, as shown in Figs. 22f, g, display nucleation of DRX grains along the grain boundaries of the elongated grains. The increase in temperature has changed the deformation mechanism from work hardening to simultaneous recrystallization of grains along the grain boundaries. Formation of shear bands, if any, will be alleviated through dynamic recrystalliation along these bands. The high strain rate ($10s^{-1}$) and high temperature have enough driving force to facilitate nucleation along the grain boundaries. The band contrast image and the recrystallization fraction map as shown in Figs. 23b,d confirm the recrystallization of grains.

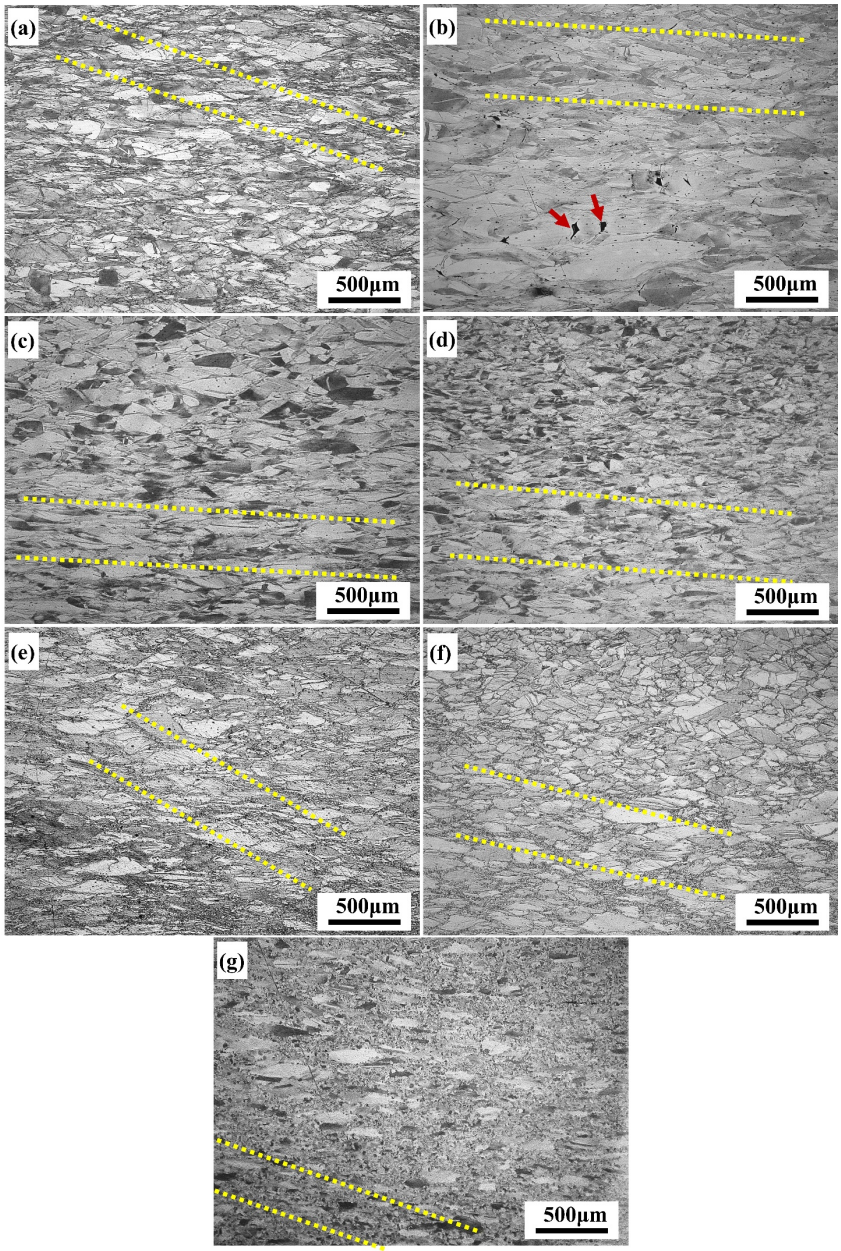

Fig. 22: Micrographs of CoCrFeMnNi HEA deformed at; a) 1023K/10s^{-1}; b) 1073K/10s^{-1}; c) 1123K/10s^{-1}; d) 1173K/10s^{-1}; e) 1223K/10s^{-1}; f) 1273K/10s^{-1}; g) 1323K/10s^{-1}.

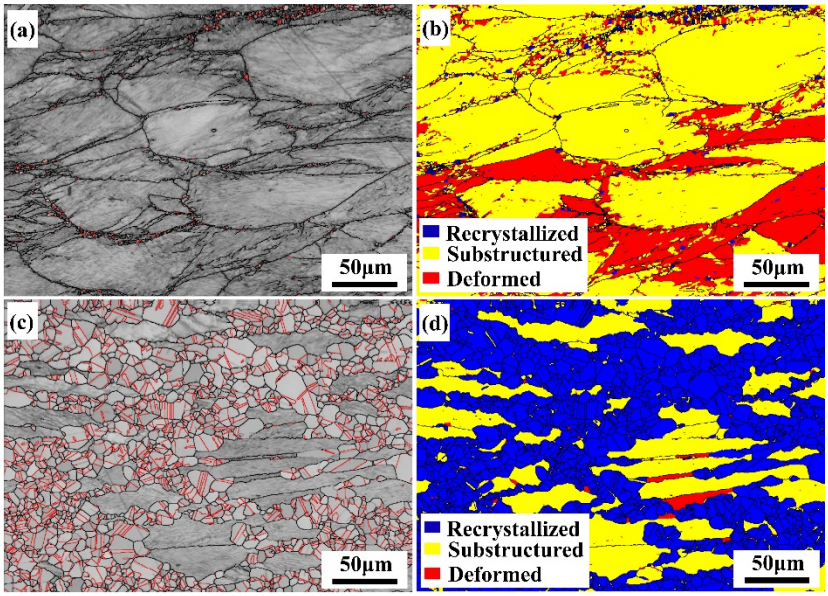

Fig. 23: (a), (c) Band contrast images of specimens tested at 1123K/10s^{-1} and 1323K/10s^{-1}; (b), (d) Recrystallization fraction images of specimens tested at 1123K/10s^{-1} and 1323K/10s^{-1}.

However, the high temperature plastic deformation enhanced flow localization thus forming localized shear bands. These shear bands are not adiabatic as the energy generated due to plastic deformation is utilized for nucleation along the grain boundaries.

According to the processing maps (Figs. 6a,b) the high temperature and high strain rate regime at 1423K/10 s^{-1} and 1423K/1s^{-1} test conditions with low efficiency has shown unstable flow, also marked by closely spaced contours with decreasing efficiency. It is expected that some kind of instabilities or cracking may manifest in the structure under hot deformation. Surprisingly, however, the micrograph shown in Fig. 24 depicts reconstituted microstructure with fine grains, presumably as a result of continuous recrystallization in dynamically recovered grains. However, it is seen that there is some texture suggesting a preferred orientation in some location, though obscured because of continuous recrystallization. This requires further investigation.

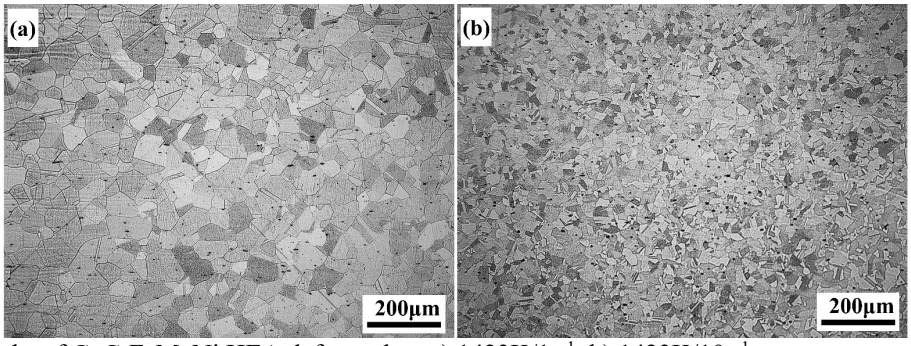

Fig. 24: Micrographs of CoCrFeMnNi HEA deformed at; a) 1423K/1s^{-1}; b) 1423K/10s^{-1}.

5.3. Conceptual processing map

Based on the outcome of the constitutive flow behavior and dynamic materials modelling supported by microstructural characterizations, a conceptual processing map is proposed for the hot working of CoCrFeMnNi HEA in the temperature range of 1023 – 1423K and strain rate range of 10^{-3} – 10s^{-1}, respectively, as shown in Fig. 25. The domain extending over the temperature range 1223 – 1373K and strain rate range 10^{-2} – 5 x $10^{-1}s^{-1}$, identified as the DRX domain, is considered 'safe' for hot working. In addition, the domain at high strain rate and high temperature (1373K/10s^{-1}) shows continuous recrystallization that could potentially be used for hot working without any microstructural defects. The other domains are not safe for hot working due to the formation of defects like localized flow, shear bands, voids, grain boundary cracking, etc., as explained in the previous sections. It should also be emphasized that the domain/regime boundaries demarcated in the processing map, as shown in Fig. 25, are only approximate. The dimensionless parameters (η and ξ) and microstructural evolutions of different domains and regimes explained below are categorized in Table 2.

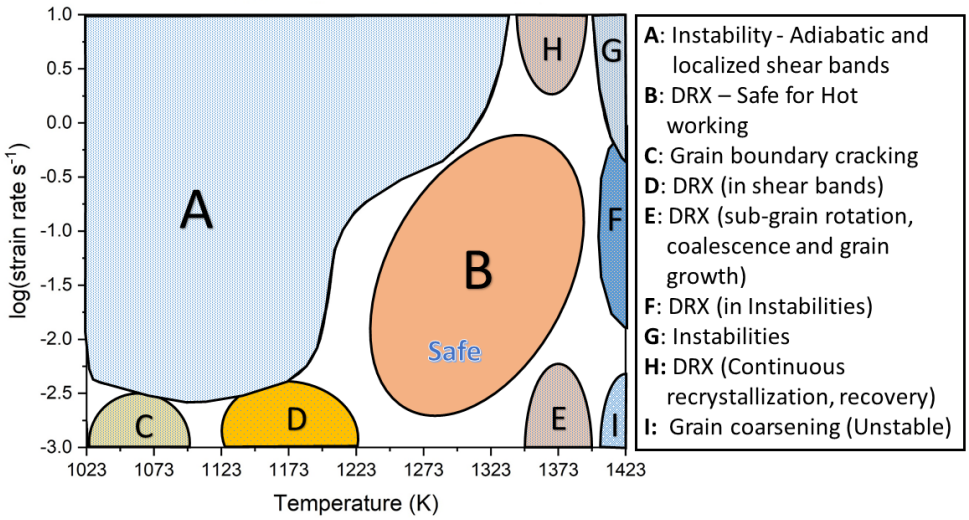

Fig 25: Processing map of Hot rolled CoCrFeMnNi HEA at true strain = 0.6.

Table 2: Summary of deformation mechanisms occurring at different domains at true strain = 0.6

Region	**T range (K)**	**$\dot{\varepsilon}$ range (s^{-1})**	**η range (%)**	**ξ range (value)**	**key microstructural features**	**Broad Mechanism**
A	1023 – 1323 (Instability regime)	10^{-2} – 10	8 – 32	-0.61 to 0.49	Voids, adiabatic shear band, GB cracking/sliding, localized shear bands	Manifestation of instabilities
B	1223 – 1373 (Deterministic domain)	10^{-2} – 5×10^{-1}	27 - 34	0.12 to 0.26	Recrystallization and grain growth	DRX - safe for hot working
C	1023 – 1098	10^{-3} – 3×10^{-3}	23 - 36	-0.22 to 0.06	GB cracking/ sliding, equi-axed fine grains at the grain boundaries	Instability
D	1123 – 1223	10^{-3} – 3×10^{-3}	32 - 48	-0.39 to 0.16	Flow localized shear band	Instability
E	1348 – 1403	10^{-3} – 3×10^{-3}	25 - 38	0.13 to 0.32	Subgrain rotation, coalescence and grain growth	DRX - not safe for working
F	1398 – 1423	10^{-2} – 3×10^{-1}	32 - 44	0.08 to 0.66	Recrystallization and grain growth	DRX - not safe for working
G	1348 – 1398	3 – 10	28 - 34	0.02 to 0.3	Continuous recrystallization	DRX - potential safe workable domain
H	1398 – 1423 (Instability regime)	3×10^{-1} – 10	5 - 42	-0.95 to 0.13	Continuous recrystallization, recovery	Unstable flow
I	1400 – 1423	10^{-3} – 3×10^{-3}	5 - 27	0.49 to 0.88	Grain coarsening	Instability

Table 3: Comparison of the current work with previous works on similar and other high entropy alloys

	CoCrFeMnNi (Current Work)	**CoCrFeMnNi** [21]	**CoCuFeMnNi** [22]	**CoCuFeNiTi** [23]
Test temperatures (K)	1023, 1073, 1123, 1173, 1223, 1273, 1323, 1373 and 1423	1023, 1098 ,1173, 1248 and 1323	1123, 1173, 1223, 1273 and 1323	1073, 1173, 1223, 1273
Strain rate ranges (s^{-1})	10^{-3}, 10^{-2}, 10^{-1}, 1 and 10	10^{-3}, 10^{-2}, 10^{-1}, 1 and 10	10^{-3}, 10^{-2}, 10^{-1}, 1 and 10	10^{-3}, 10^{-2} and 10^{-1}
In-depth analysis along with microstructural correlation	Mechanisms operating in different domains clarified along with microstructural validation	No proper microstructural correlation with the predictions of the domains	Four domains explained with optical micrographs and EBSD analysis	Three domains explained using SEM and TEM examination
As received condition	Hot rolled at 1273K; average grain size ~ 13 μm	As-cast and homogenized; average grain size ~ 419μm	As-cast and homogenized; initial grain size not mentioned	As-cast samples; initial grain size not mentioned
Instability Map based on	Prasad's Criteria [32]	Murthy's Criteria [37]	Prasad's Criteria [32]	Prasad's Criteria [32]
Identification of 'safe' hot working domain	Deterministic domain 1223 – 1373K and $10^{-2} – 5\times10^{-1}$ s^{-1} with $\boldsymbol{\eta}$ ~ (27 – 34) %	The deterministic domain associated with $\eta \geq 30\%$ occurs between 1173 – 1323 K and strain rate range $10^{-3} – 10^{-1}$ s^{-1}; best hot working condition 1323 K/10^{-3} s^{-1}	Best hot workability domain is extending over 1123K - 1223K at $10^{-1}s^{-1}$ with η ~20 – 25 %	Optimum safe working condition in the temperature range 1203 – 1263 K and strain rate range 10^{-3} s^{-1} – 10^{-1} s^{-1}.
Microstructural features in safe working domain	DRX and grain growth	DRX occurrence mentioned; but not correlated with the safe working domain	Formation of DRX grains within shear band	Uniform distribution of phases in the safe working domain, free from voids and cracks
Instability regime	Corroborated well with the microstructural analysis from each of the instability regions	Instability regime presumed based on the instability parameter	No clear explanation of instability regime except mentioned in the processing map	Instability regime identified as 1073–1093K and 10^{-2} –10^{-1} s^{-1}; correlated with microstructures
Microstructural features in instability regime	GB cracking, voids, adiabatic shear bands, flow localization with	Flow localization with shear bands	Cavity and shear band formation	Pores, localized flow, large cracks and small

	shear bands and subgrain coalescence			pieces near cracks

From the above comparison (Table 3), it is clear that the current study on the hot working behavior of CoCrFeMnNi high entropy alloy is quite comprehensive extending over a wide range of temperatures and strain rates in comparison to previous studies. Various deterministic domains and instability regimes have been systematically characterized in this study, whereas other studies limited their characterization to few domains. A safe hot working window has also been identified in the present study based on the outcome of the processing map, corroborated with in-depth microstructural analysis, in comparison to previous works [21–23].

6. Conclusion

In this study, the constitutive flow behavior of a hot rolled CoCrFeMnNi HEA has been assessed in the hot working temperature range of 1023 – 1423K and strain rate range of 10^{-3} – $10s^{-1}$ using the principles of DMM. A processing map was developed defining different domains and the instability regime showing various microstructural mechanisms. Additionally, a 'safe' processing window for the hot working of the alloy was identified. Based on the observations made from the processing map, supported by extensive microstructural analysis, the following conclusions can be drawn:

1. The domain extending over the temperature (1223 – 1373K) and strain rate (10^{-2} – 5×10^{-1} s^{-1}) ranges, identified as the DRX domain, is considered 'safe' for hot working.
2. The high temperatures above 1403K at all tested strain rates are not safe for hot working because the steep increase/decrease in efficiency with close contours can likely lead to intergranular cracking.
3. The temperatures below 1223K at all strain rates fall in the instability regime and is considered unsafe for hot working.
4. There is a small window of temperature (1348 – 1398K) at high strain rates (3 – 10 s^{-1}), that could presumably be used for near-isothermal hot working without the occurrence of any microstructural defects, though it may extend to higher strain rates. However, further investigation is required to determine the detailed characteristics of this domain.
5. The CoCrFeMnNi is also prone to various microstructural defects such as GB cracking/sliding, voids formation, formation of shear bands through flow localization and adiabatic shear bands. These defects are exhibited by microstructures in the instability regimes.

Acknowledgements

This study was performed with the support of Tampere University Foundation as a part of Tampere university graduate school. The microstructural characterization was carried out using the facilities at the Tampere Microscopy Center, Tampere University. We sincerely thank Mr. Jussi Paavola and Mr. Juha Uusitalo of Oulu university for conducting meticulously the laboratory hot rolling of the HEA and isothermal compression tests in the Gleeble simulator, respectively.

Data availability statement

The raw data required to reproduce these finding cannot be shared at this time as the data also forms part of an ongoing study.

References

[1] J.-W. Yeh, S.-K. Chen, S.-J. Lin, J.-Y. Gan, T.-S. Chin, T.-T. Shun, C.-H. Tsau, S.-Y. Chang, Nanostructured High-Entropy Alloys with Multiple Principal Elements: Novel Alloy Design

Concepts and Outcomes, Advanced Engineering Materials. 6 (2004) 299–303. https://doi.org/10.1002/adem.200300567.
[2] Z. Li, A. Ludwig, A. Savan, H. Springer, D. Raabe, Combinatorial metallurgical synthesis and processing of high-entropy alloys, Journal of Materials Research. 33 (2018) 3156–3169. https://doi.org/10.1557/jmr.2018.214.
[3] D.B. Miracle, O.N. Senkov, A critical review of high entropy alloys and related concepts, Acta Materialia. 122 (2017) 448–511. https://doi.org/10.1016/j.actamat.2016.08.081.
[4] B. Cantor, I.T.H. Chang, P. Knight, A.J.B. Vincent, Microstructural development in equiatomic multicomponent alloys, Materials Science and Engineering: A. 375–377 (2004) 213–218. https://doi.org/10.1016/j.msea.2003.10.257.
[5] F. Otto, A. Dlouhý, K.G. Pradeep, M. Kuběnová, D. Raabe, G. Eggeler, E.P. George, Decomposition of the single-phase high-entropy alloy CrMnFeCoNi after prolonged anneals at intermediate temperatures, Acta Materialia. 112 (2016) 40–52. https://doi.org/10.1016/j.actamat.2016.04.005.
[6] B. Schuh, F. Mendez-Martin, B. Völker, E.P. George, H. Clemens, R. Pippan, A. Hohenwarter, Mechanical properties, microstructure and thermal stability of a nanocrystalline CoCrFeMnNi high-entropy alloy after severe plastic deformation, Acta Materialia. (2015). https://doi.org/10.1016/j.actamat.2015.06.025.
[7] E.J. Pickering, R. Muñoz-Moreno, H.J. Stone, N.G. Jones, Precipitation in the equiatomic high-entropy alloy CrMnFeCoNi, Scripta Materialia. 113 (2016) 106–109. https://doi.org/10.1016/j.scriptamat.2015.10.025.
[8] E.P. George, D. Raabe, R.O. Ritchie, High-entropy alloys, Nature Reviews Materials. 4 (2019). https://doi.org/10.1038/s41578-019-0121-4.
[9] F. Otto, N.L. Hanold, E.P. George, Microstructural evolution after thermomechanical processing in an equiatomic, single-phase CoCrFeMnNi high-entropy alloy with special focus on twin boundaries, Intermetallics. 54 (2014) 39–48. https://doi.org/10.1016/j.intermet.2014.05.014.
[10] J.Y. He, C. Zhu, D.Q. Zhou, W.H. Liu, T.G. Nieh, Z.P. Lu, Steady state flow of the FeCoNiCrMn high entropy alloy at elevated temperatures, Intermetallics. 55 (2014) 9–14. https://doi.org/10.1016/j.intermet.2014.06.015.
[11] N.D. Stepanov, D.G. Shaysultanov, N.Y. Yurchenko, S.V. Zherebtsov, A.N. Ladygin, G.A. Salishchev, M.A. Tikhonovsky, High temperature deformation behavior and dynamic recrystallization in CoCrFeNiMn high entropy alloy, Materials Science and Engineering: A. 636 (2015) 188–195. https://doi.org/10.1016/j.msea.2015.03.097.
[12] R.R. Eleti, T. Bhattacharjee, L. Zhao, P.P. Bhattacharjee, N. Tsuji, Hot deformation behavior of CoCrFeMnNi FCC high entropy alloy, Materials Chemistry and Physics. 210 (2018) 176–186. https://doi.org/10.1016/j.matchemphys.2017.06.062.
[13] M.C. Somani, N.C. Birla, Y.V.R.K. Prasad, V. Singh, Microstructural validation of processing maps using the hot extrusion of P/M Nimonic AP-1 superalloy, Journal of Materials Processing Technology. 52 (1995) 225–237. https://doi.org/10.1016/0924-0136(94)01609-5.
[14] C.M. Sellars, HOT WORKING, in: Materials Engineering, Elsevier, 1986: pp. 231–243. https://doi.org/10.1016/B978-0-08-033454-7.50019-X.
[15] R. Raj, DEVELOPMENT OF A PROCESSING MAP FOR USE IN WARM-FORMING AND HOT-FORMING PROCESSES., Metallurgical Transactions. A, Physical Metallurgy and Materials Science. (1981). https://doi.org/10.1007/BF02643490.
[16] M.F. Ashby, A first report on deformation-mechanism maps, Acta Metallurgica. (1972). https://doi.org/10.1016/0001-6160(72)90082-X.
[17] Y.V.R.K. Prasad, H.L. Gegel, S.M. Doraivelu, J.C. Malas, J.T. Morgan, K.A. Lark, D.R. Barker, Modeling of dynamic material behavior in hot deformation: Forging of Ti-6242, Metallurgical Transactions A. (1984). https://doi.org/10.1007/BF02664902.
[18] M.C. Somani, E.S.B. Rao, N.C. Birla, M.L. Bhatia, V. Singh, Y.V.R.K. Prasad, Processing map for controlling microstructure in hot working of hot isostatically pressed powder metallurgy NIMONIC AP-1 superalloy, Metallurgical Transactions A. (1992). https://doi.org/10.1007/BF02651762.
[19] J.K. Chakravartty, Y.V.R.K. Prasad, M.K. Asundi, Processing map for hot working of alpha-zirconium, Metallurgical Transactions A. (1991). https://doi.org/10.1007/BF02658992.
[20] Y.V.R.K. Prasad, T. Seshacharyulu, Processing maps for hot working of titanium alloys, Materials Science and Engineering A. (1998). https://doi.org/10.1016/s0921-5093(97)00782-x.
[21] H.T. Jeong, H.K. Park, K. Park, T.W. Na, W.J. Kim, High-temperature deformation mechanisms and processing maps of equiatomic CoCrFeMnNi high-entropy alloy, Materials Science and Engineering:

A. 756 (2019) 528–537. https://doi.org/10.1016/J.MSEA.2019.04.057.
[22] N. Prasad, N. Bibhanshu, N. Nayan, G.S. Avadhani, S. Suwas, Hot deformation behavior of the high-entropy alloy CoCuFeMnNi, Journal of Materials Research. 34 (2019) 744–755. https://doi.org/DOI: 10.1557/jmr.2018.500.
[23] S. Samal, M.R. Rahul, R.S. Kottada, G. Phanikumar, Hot deformation behaviour and processing map of Co-Cu-Fe-Ni-Ti eutectic high entropy alloy, Materials Science and Engineering A. (2016). https://doi.org/10.1016/j.msea.2016.04.006.
[24] H. Rastegari, A. Kermanpur, A. Najafizadeh, D. Porter, M. Somani, Warm deformation processing maps for the plain eutectoid steels, Journal of Alloys and Compounds. (2015). https://doi.org/10.1016/j.jallcom.2014.11.170.
[25] Y.V.R.K. Prasad, T. Seshacharyulu, Modelling of hot deformation for microstructural control, International Materials Reviews. (2014). https://doi.org/10.1179/imr.1998.43.6.243.
[26] H. Ziegler, Progress in solid mechanics, New York: Wiley. 63 (1963).
[27] M. Patnamsetty, A. Saastamoinen, M.C. Somani, P. Peura, Constitutive modelling of hot deformation behaviour of a CoCrFeMnNi high-entropy alloy, Science and Technology of Advanced Materials. 21 (2020) 43–55. https://doi.org/10.1080/14686996.2020.1714476.
[28] D.-X. Wen, Y.C. Lin, H.-B. Li, X.-M. Chen, J. Deng, L.-T. Li, Hot deformation behavior and processing map of a typical Ni-based superalloy, Materials Science and Engineering: A. 591 (2014) 183–192. https://doi.org/10.1016/j.msea.2013.09.049.
[29] S. Huang, W. Li, S. Lu, F. Tian, J. Shen, E. Holmström, L. Vitos, Temperature dependent stacking fault energy of FeCrCoNiMn high entropy alloy, Scripta Materialia. 108 (2015) 44–47. https://doi.org/http://dx.doi.org/10.1016/j.scriptamat.2015.05.041.
[30] A.J. Zaddach, C. Niu, C.C. Koch, D.L. Irving, Mechanical properties and stacking fault energies of NiFeCrCoMn high-entropy alloy, JOM. 65 (2013) 1780–1789. https://doi.org/10.1007/s11837-013-0771-4.
[31] H. Mirzadeh, J.M. Cabrera, A. Najafizadeh, P.R. Calvillo, EBSD study of a hot deformed austenitic stainless steel, Materials Science and Engineering A. (2012). https://doi.org/10.1016/j.msea.2012.01.037.
[32] Y.V.R.K. Prasad, K.P. Rao, S. Sasidhar, Hot Working Guide: A Compendium of Processing Maps, Second Edition - Google Books, 2015.
[33] M.A. Meyers, Plasticity: Adiabatic Shear Localization, Encyclopedia of Materials: Science and Technology. (2001) 7093–7103. https://doi.org/10.1016/B0-08-043152-6/01257-2.
[34] R.C. Gifkins, Grain-boundary participation in high-temperature deformation: An historical review, Materials Characterization. (1994). https://doi.org/10.1016/1044-5803(94)90093-0.
[35] F.J. Humphreys, M. Hatherly, Chapter 14 - Continuous Recrystallization During and after Large Strain Deformation, in: F.J. Humphreys, M.B.T.-R. and R.A.P. (Second E. Hatherly (Eds.), Elsevier, Oxford, 2004: pp. 451–467. https://doi.org/https://doi.org/10.1016/B978-008044164-1/50018-9.
[36] M.C. Somani, K. Muraleedharan, Y.V.R.K. Prasad, V. Singh, Mechanical processing and microstructural control in hot working of hot isostatically pressed P/M IN-100 superalloy, Materials Science and Engineering: A. 245 (1998) 88–99. https://doi.org/10.1016/S0921-5093(97)00698-9.
[37] S.V.S.N. Murty, M.S. Sarma, B.N. Rao, On the evaluation of efficiency parameters in processing maps, Metallurgical and Materials Transactions A: Physical Metallurgy and Materials Science. (1997). https://doi.org/10.1007/s11661-997-0219-y.